

Quantum-Assisted Support Vector Regression for Detecting Facial Landmarks

Archismita Dalal,^{*} Mohsen Bagherimehrab,[†] and Barry C. Sanders[‡]

Institute for Quantum Science and Technology, University of Calgary, Alberta T2N 1N4, Canada

(Dated: November 18, 2021)

The classical machine-learning model for support vector regression (SVR) is widely used for regression tasks, including weather prediction, stock-market and real-estate pricing. However, a practically realisable quantum version for SVR remains to be formulated. We devise annealing-based algorithms, namely simulated and quantum-classical hybrid, for training two SVR models, and compare their empirical performances against the SVR implementation of Python’s scikit-learn package and the SVR-based state-of-the-art algorithm for the facial-landmark-detection (FLD) problem. Our method is to derive a quadratic-unconstrained-binary formulation for the optimisation problem used for training a SVR model and solve this problem using annealing. Using D-Wave’s Hybrid Solver, we construct a quantum-assisted SVR model, thereby demonstrating a slight advantage over classical models regarding landmark-detection accuracy. Furthermore, we observe that annealing-based SVR models predict landmarks with lower variances compared to the SVR models trained by greedy optimisation procedures. Our work is a proof-of-concept example for applying quantum-assisted SVR to a supervised learning task with a small training dataset.

I. INTRODUCTION

The classical machine-learning model for support vector regression (SVR) is widely used for regression tasks, including prediction of weather, stock market and real-estate pricing [1–5]. However, a practically realisable quantum version for SVR is yet to be established in the quantum machine-learning domain [6, 7]. Current feasible applications of quantum machine learning employ quantum annealing [8] to enhance one of the essential components in machine learning, i.e. optimisation problem. Consequently, these quantum-assisted solutions are shown, empirically, to be slightly more accurate than classical solutions [9–11]. Our aim here is to devise a quantum-assisted SVR model by employing D-Wave’s quantum-classical hybrid solvers [12], and compare this quantum-assisted model against classical models for detecting facial landmarks, e.g., centres of eyes, nose tip and corners of the mouth, in unconstrained images [13].

We state the facial landmark detection (FLD) task, along with its applications, computational challenges and state-of-the-art methods to accurately perform this task. The task of FLD is to identify key landmarks on a human-face image [13, 14], with important applications such as face recognition [15–17], three-dimensional face reconstruction [18], facial-emotion recognition [19] and gender prediction [20]. Efficient and robust FLD is challenging due to large variability of appearance, expression, illumination and partial occlusion of unconstrained face images, i.e., images obtained in uncontrolled conditions [13]. Neural regression-based algorithms are considered the state-of-the-art in FLD as they deliver the highest detection accuracies so far [21, 22].

We introduce a quantum-assisted model to enhance the regression performance of SVR and further utilise FLD as a proof-of-principle application. The detection accuracy of a FLD algorithm is typically limited by the size and quality of training data and computational resources available [22]. To this end, we test if quantum resources can enhance the performance of our SVR-based FLD algorithm for the case of a small training dataset comprising 100 unconstrained face images. We use a limited-size training dataset for two reasons: feasibility on current quantum hardware and the success of other quantum machine-learning applications [9–11] with limited-size datasets. Our FLD algorithm only serves as a test case for our quantum-assisted SVR formulation and does not directly advance the state-of-the-art in FLD algorithms [22].

Quantum-assisted algorithms are exhibited as superior alternatives to classical algorithms for classification tasks, including the protein-binding problem in computational biology [10, 11] and the Higgs particle-classification problem in high-energy physics [9]. One such promising classification model is a quantum-assisted support vector machine (SVM), which is mathematically similar to SVR and makes use of support vectors to train a classification model [23]. The support vectors are calculated by solving a constrained optimisation problem using quantum annealing [11], as opposed to using greedy optimisation routines in `scikit-learn` [24]. D-Wave Systems’ practical quantum annealing machine, commonly called an annealer, solves this optimisation problem by casting it as an Ising minimisation, or equivalently, quadratic unconstrained binary optimisation (QUBO) problem. The classification accuracy of a SVM model, trained with a limited-size training dataset, for the task of protein binding is improved using an ensemble of close-to-optimal solutions obtained from D-Wave’s quantum annealer [11].

Whereas D-Wave’s quantum annealer has many applications, there are some limitations on its implementation of quantum annealing and its broader usability.

^{*} archismita.dalal@ucalgary.ca

[†] mohsen.bagherimehrab@ucalgary.ca

[‡] sandersb@ucalgary.ca

The solution from the annealer is not deterministic, and the device’s noise further degrades the quality of the solution. Although the state-of-the-art quantum annealer comprises about 5000 qubits, this device can solve optimisation problems with up to 108 variables, which correspond to fully connected graphs, due to restricted connectivity in its hardware. As empirical evidence for quantum speedup with D-Wave’s annealer is still under investigation, machine learning tasks are assessed using other performance metrics [10, 11]. Moreover, recent applications employ D-Wave’s quantum-classical hybrid annealing, which can tackle problems with a million variables [25, 26].

We develop a quantum-classical hybrid machine-learning algorithm to solve the FLD problem and execute this algorithm on a D-Wave’s quantum annealer. Methodologically, we split the multi-output regression task for FLD [27] into several single-output regressions and then train a SVR model for each single-output regression problem. We derive a QUBO formulation for the constrained optimisation problem associated with the training of each SVR model and solve this QUBO problem using both classical annealing and hybrid approaches. Having constructed the quantum-assisted and classical models, we then assess and compare the statistical significance of their detection accuracies for FLD. We observe that the annealing-based SVR models predict landmarks with lower variance compared to the SVR models trained by greedy optimisation procedures [28, 29].

Our paper is organized as follows. We begin in §II by elaborating the pertinent background for SVR, FLD and quantum annealing on D-Wave. In §III, we describe our approach for solving the FLD problem using quantum-assisted SVR models and elaborate on the steps of the associated machine-learning workflow. We then present our results in §IV, where we derive a QUBO formulation for SVR and compare the performance of our quantum-assisted approach against the classical approaches for FLD. Finally, we discuss our results and their implications in §V, and conclude in §VI.

II. BACKGROUND

In this section, we discuss the relevant background for SVR machines, regression-based FLD and practical quantum annealing. We begin, in §II A, by explaining the supervised-learning problem of regression and the SVR model. Then, in §II B, we present the landmark-detection problem as a supervised learning problem of regression, along with its standard performance metrics. In the final subsection §II C, we describe the concepts of quantum annealing and its implementation by D-Wave Systems.

A. Support vector regression

We now review the key background pertinent to SVR [1, 2]. A SVR has two formulations known as ‘primal’ and ‘dual’. We start by describing the primal formulation of a linear SVR in §II A 1, followed by its dual formulation in §II A 2. Finally, we discuss the kernel method that is used to deal with nonlinear regression in §II A 3.

1. Primal formulation

Here we discuss the primal formulation of a linear SVR. First we describe SVR as a tool for solving the supervised-learning problem of regression. Then we discuss the associated constrained optimisation problem required in training a SVR model.

For a supervised-learning problem of single-output regression, we are given a training dataset with M data points. Each data point is a tuple (\mathbf{x}_i, y_i) , where \mathbf{x}_i is a real-valued feature vector of dimension F and y_i is the target value of \mathbf{x}_i . The dataset is formally stated as

$$\mathcal{D}_{\text{SVR}} = \{(\mathbf{x}_i, y_i) \mid i \in [M] := \{0, \dots, M-1\}\} \subset \mathbb{R}^F \times \mathbb{R}. \quad (1)$$

The learning problem involves estimating a prediction function $f(\mathbf{x})$ for an unseen feature vector \mathbf{x} , such that the estimated target is $\tilde{y} = f(\mathbf{x})$. SVR is a powerful and robust method to address this learning problem [1, 2]. For \mathbf{w} the normal vector to a hyperplane and b the offset, the task in the linear SVR is to search for a linear prediction function

$$f_{\text{linear}}(\mathbf{x}) = \mathbf{w} \cdot \mathbf{x} + b \quad (\mathbf{w} \in \mathbb{R}^F, b \in \mathbb{R}), \quad (2)$$

such that, for a given error tolerance $\varepsilon \in \mathbb{R}^+$,

$$|f_{\text{linear}}(\mathbf{x}_i) - y_i| \leq \varepsilon \quad \forall i \in [M], \quad (3)$$

while minimizing the norm $\|\mathbf{w}\|^2 = \mathbf{w} \cdot \mathbf{w}$ [2]. This formulation is also known as ε -SVR, where ε is the error tolerance in Eq. (3).

The linear ε -SVR is formally written as the convex-optimisation problem

$$\min_{\mathbf{w}, b} \left\{ \frac{\mathbf{w}^2}{2} \mid |\mathbf{w} \cdot \mathbf{x}_i + b - y_i| \leq \varepsilon \quad \forall i \in [M] \right\}. \quad (4)$$

This optimisation problem might not be feasible; i.e. it is possible that no linear function $f(\mathbf{x})$ (2) exists to satisfy the constraint in Eq. (3) for all training data points (1). In order to cope with this infeasibility issue, analogous to the soft-margin concept in support vector machine classification [23], slack variables are used. Specifically, in the soft-margin ε -SVR, two slack variables $\xi^+, \xi^- \in (\mathbb{R}^+)^M$ are introduced for each training point¹; see Fig. 1. Intro-

¹ If we use one slack variable then the constraints in the optimi-

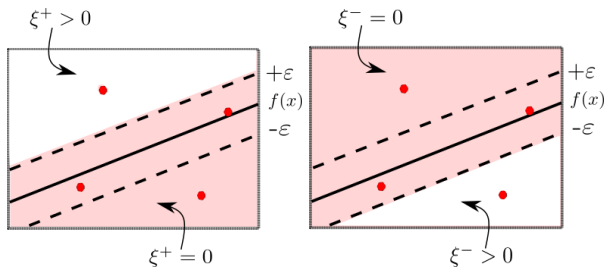


FIG. 1. Two slack variables ξ^+ and ξ^- are used in an ε -SVR formulation. Red circles are data points. (left) $\xi^+ = 0$ if the corresponding training data point is below the upper bound and $\xi^+ > 0$ if it is above the upper bound, (right) $\xi^- = 0$ if the corresponding training data point is above the lower bound and $\xi^- > 0$ if it is below the lower bound.

ducing these slack variables and a regularisation hyperparameter $\gamma \in \mathbb{R}^+$ leads to the optimisation problem

$$\min_{\substack{\mathbf{w}, b \\ \xi^+, \xi^-}} \left\{ \frac{\mathbf{w}^2}{2} + \gamma \|\xi^+ + \xi^-\|_1 \right\}, \quad (5)$$

subject to the inequality constraints

$$-\varepsilon - \xi_i^+ \leq \mathbf{w} \cdot \mathbf{x}_i + b - y_i \leq \varepsilon + \xi_i^- \quad \forall i \in [M]. \quad (6)$$

The optimisation problem in Eq. (5) is known as the primal formulation of ε -SVR. The regularization hyperparameter γ in this equation determines trade-off between minimizing the norm $\|\mathbf{w}\|$, i.e., the flatness of the function $f(\mathbf{x})$, and the amount by which deviations greater than the error ε are tolerated.

2. Dual formulation

We now proceed to describe the dual formulation of a linear ε -SVR. First we explain how to derive the dual formulation of the optimisation problem of ε -SVR from its primal formulation (5). Then we obtain an expression for the linear ε -SVR model, i.e., the prediction function, in terms of the variables in the dual formulation. The dual formulation of a ε -SVR is a two-variable optimisation problem, where one variable represents one Lagrange multiplier vector, which we finally express as a single-variable optimisation problem.

In the dual formulation, we construct a Lagrange function from the objective function (5) and the constraints (6) of the primal optimisation problem using Lagrange multiplier vectors $\boldsymbol{\alpha}^+, \boldsymbol{\alpha}^- \in (\mathbb{R}^+)^M$. Lagrange equations are obtained by taking partial derivatives of

sation problem would be absolute value of some function and therefore the constraints would be non-differentiable. In this case deriving the dual formulation or the KKT conditions will be cumbersome.

Lagrange function with respect to the variables \mathbf{w}, ξ^+, ξ^- and b and then setting these equations to zero. This procedure yields an expression for \mathbf{w} in terms of $\boldsymbol{\alpha}^+, \boldsymbol{\alpha}^-$ as

$$\mathbf{w} = (\boldsymbol{\alpha}^+ - \boldsymbol{\alpha}^-) \cdot \mathbf{X}, \quad (7)$$

where \mathbf{X} is a vector that comprises the feature vectors $\{\mathbf{x}_i\}$ in Eq. (1) as its components, and constraints

$$\|\boldsymbol{\alpha}^+\|_1 = \|\boldsymbol{\alpha}^-\|_1, \quad 0 \leq \alpha_i^+, \alpha_i^- \leq \gamma \quad \forall m \in [M], \quad (8)$$

on $\boldsymbol{\alpha}^+$ and $\boldsymbol{\alpha}^-$. The optimisation problem in the dual formulation of ε -SVR is

$$\min_{\boldsymbol{\alpha}^+, \boldsymbol{\alpha}^-} \left\{ \frac{1}{2} (\boldsymbol{\alpha}^+ - \boldsymbol{\alpha}^-)^\top \mathbf{K} (\boldsymbol{\alpha}^+ - \boldsymbol{\alpha}^-) + \varepsilon \|\boldsymbol{\alpha}^+ + \boldsymbol{\alpha}^-\|_1 - \mathbf{y} \cdot (\boldsymbol{\alpha}^+ - \boldsymbol{\alpha}^-) \right\}, \quad (9)$$

for $\mathbf{K} = (K_{ij}) \in \mathbb{R}^{M \times M}$ with $K_{ij} := \mathbf{x}_i \cdot \mathbf{x}_j$, subject to the constraints in Eq. (8). The solution of this optimisation problem is the two Lagrange multiplier vectors $\boldsymbol{\alpha}^+$ and $\boldsymbol{\alpha}^-$. Only a few of the Lagrange multipliers are nonzero: these are the ones corresponding to data points that specify the prediction function, which are known as support vectors.

The linear prediction function (2) is now expressed in terms of the Lagrange multipliers and offset b as

$$f_{\text{linear}}(\mathbf{x}) = \sum_{i=0}^{M-1} (\alpha_i^+ - \alpha_i^-) \mathbf{x}_i \cdot \mathbf{x} + b, \quad (10)$$

where b is calculated using the two Lagrange multiplier vectors $\boldsymbol{\alpha}^+$ and $\boldsymbol{\alpha}^-$; see Appendix A. This function is commonly referred to as the linear ε -SVR model.

Now we explain the standard method to convert the two-variable optimisation problem (9) into a single-variable problem [1]. This is done by defining a new Lagrange multiplier vector $\boldsymbol{\alpha}$, whose elements relate to the two old Lagrange multiplier vectors $\boldsymbol{\alpha}^+$ and $\boldsymbol{\alpha}^-$ as

$$\alpha_i := \alpha_i^+, \quad \alpha_{M+i} := \alpha_i^- \quad \forall i \in [M]. \quad (11)$$

Additionally, \mathbf{y} and ε are replaced by a single new variable \mathbf{c} as

$$c_i := \varepsilon - y_i, \quad c_{M+i} := \varepsilon + y_i \quad \forall i \in [M], \quad (12)$$

and a $2M \times 2M$ symmetric matrix \mathbf{Q} is introduced as

$$\mathbf{Q} := \begin{bmatrix} \mathbf{K} & -\mathbf{K} \\ -\mathbf{K} & \mathbf{K} \end{bmatrix}, \quad (13)$$

with \mathbf{K} the kernel matrix in Eq. (9). In terms of the new variables $\boldsymbol{\alpha}$ and \mathbf{c} , the one-variable optimisation problem in the dual form is

$$\min_{\boldsymbol{\alpha}} \left\{ \frac{1}{2} \boldsymbol{\alpha}^\top \mathbf{Q} \boldsymbol{\alpha} + \boldsymbol{\alpha} \cdot \mathbf{c} \right\}, \quad (14a)$$

$$\sum_{i=0}^{M-1} \alpha_i = \sum_{i=M}^{2M-1} \alpha_i, \quad \alpha_i \in [0, \gamma] \quad \forall i \in [2M]. \quad (14b)$$

Due to the quadratic nature of this optimisation problem, the solution to this problem is a unique Lagrange multiplier vector $\boldsymbol{\alpha} \in \mathbb{R}^{2M}$. This vector is then used to compute the offset b , as described in Appendix A, which together with $\boldsymbol{\alpha}$ specify the prediction function $f_{\text{linear}}(\boldsymbol{x})$ (10).

3. Kernel method for nonlinear data

We now explain the formulation of a nonlinear extension of ε -SVR using a method known as the kernel method; see [30, Sec. 7.4] for details. We begin with describing the concept of ‘feature mapping’ as a convenient way to deal with nonlinear regression problems in the framework of linear ε -SVR. Then we build upon the feature mapping and describe the kernel method as a computationally efficient method to deal with nonlinear data through kernel functions. Finally, we state commonly used kernel functions in the kernel method.

Feature mapping is an approach for applying the linear ε -SVR formulation to nonlinear regression problems. In this approach, vectors of the input feature space are first embedded into a space of equal or higher-dimension by a feature map² defined as

$$\text{embed} : \mathbb{R}^F \rightarrow \mathbb{R}^{F'} : \boldsymbol{x}_m \mapsto \text{embed}(\boldsymbol{x}_m) \quad \forall F' \geq F \quad (15)$$

and then a linear ε -SVR model (10) is constructed using the embedded feature vectors. To accommodate nonlinear data, the feature-mapping approach requires an explicitly defined feature map **embed** (15) and becomes computationally inefficient as F' increases.

Kernel method bypasses the embedding in feature mapping and provides a computationally efficient way to extend the linear ε -SVR to nonlinear data. This approach relies on the observation that the optimisation problem (9) in the dual formulation and the prediction function (10) depend only on the dot product between the feature vectors. Therefore, we only need to know the dot product between the embedded vectors **embed**(\boldsymbol{x}_m) rather than the feature map **embed** (15) itself to construct a prediction model. In kernel methods, the dot product between the embedded vectors is computed by a kernel function defined as

$$\begin{aligned} K : \mathbb{R}^F \times \mathbb{R}^F &\rightarrow \mathbb{R}, \\ (\boldsymbol{x}_n, \boldsymbol{x}_m) &\mapsto K(\boldsymbol{x}_n, \boldsymbol{x}_m) := \text{embed}(\boldsymbol{x}_n) \cdot \text{embed}(\boldsymbol{x}_m). \end{aligned} \quad (16)$$

In the kernel method, the optimisation problem for the nonlinear ε -SVR becomes analogous to the optimisation problem (9) in the dual formulation of the linear ε -SVR

but the dot product between the feature vectors is replaced with the kernel function. Consequently, the prediction function in the kernel method becomes

$$f(\boldsymbol{x}) = \sum_{i=0}^{M-1} (\alpha_i^+ - \alpha_i^-) K(\boldsymbol{x}_i, \boldsymbol{x}) + b, \quad (17)$$

which is a nonlinear version of the linear prediction function in Eq. (10).

Finally, we state commonly used kernel functions. Three kernels are commonly used in machine-learning literature: linear, polynomial and Gaussian kernels. The linear kernel, defined as $K_L(\boldsymbol{x}_n, \boldsymbol{x}_m) := \boldsymbol{x}_n \cdot \boldsymbol{x}_m$, corresponds to trivial embedding (15) and is used for linear dataset. The polynomial kernel, for a degree- d polynomial,

$$K_P(\boldsymbol{x}_n, \boldsymbol{x}_m) = (\boldsymbol{x}_n \cdot \boldsymbol{x}_m + c)^d \quad \forall c \in \mathbb{R}, d \in \mathbb{Z}^+, \quad (18)$$

and the Gaussian kernel

$$K_G(\boldsymbol{x}_n, \boldsymbol{x}_m) = e^{-\eta|\boldsymbol{x}_n - \boldsymbol{x}_m|^2} \quad \forall \eta \in \mathbb{R}^+, \quad (19)$$

are used for nonlinear datasets. If no prior knowledge is available to determine the hyperparameter η for Gaussian kernel, its default value is chosen to be

$$\eta = 1/(F\sigma^2), \quad (20)$$

where F is the number of features and σ is the standard deviation of the given data [28].

B. Facial-landmark detection

In this subsection, we explain the relevant background on FLD. We commence by providing an overview of FLD in §II B 1, including the problem statement and regression-based algorithms for solving a FLD problem. Then, in §II B 2, we describe FLD as a machine-learning task and elaborate on the learning workflow. Finally, in §II B 3, we discuss standard benchmarking datasets and commonly used performance measures for evaluating a FLD algorithm.

1. Problem overview

Here we discuss the FLD problem. First we define the task of FLD. Then we discuss how to convert the FLD problem into a computational problem by introducing the concept of data preprocessing. Finally we elaborate on regression-based algorithms for FLD.

We begin by describing a FLD problem. First we define a ‘face shape’, which we use to describe the FLD problem. A face shape is a collection of (x, y) coordinates of a number L of key landmarks on the face; L is typically a number between 5 to 100 depending on the

² Throughout this paper we use **typewriter** font for functions and packages.

application [13]. For a truecolor face image \mathbf{I}^{raw} with L landmarks, we represent its face shape \mathbf{s}^{raw} by the vector

$$\mathbf{s}^{\text{raw}} = (s_0^{\text{raw}}, s_1^{\text{raw}}, \dots, s_{2L-1}^{\text{raw}}), \quad (21)$$

where s_{2k}^{raw} and s_{2k+1}^{raw} are real numbers denoting the manually determined values for x and y coordinates of the k th landmark, respectively. For a FLD problem, we are given a raw dataset

$$\mathcal{D}^{\text{raw}} := \{(\mathbf{I}_i^{\text{raw}}, \mathbf{s}_i^{\text{raw}}) \mid i \in [N]\} \subset \mathbb{Z}^{m \times n \times 3} \times \mathbb{R}^{2L}, \quad (22)$$

where each $\mathbf{I}_i^{\text{raw}}$ is a truecolor face image, represented by an $m \times n \times 3$ array of integers in the range $[0, 255]$ that defines red, green and blue color components for each pixel of the image³, and $\mathbf{s}_i^{\text{raw}}$ is the manually determined face shape⁴ corresponding to $\mathbf{I}_i^{\text{raw}}$. The task in FLD is to devise a model

$$\text{shape} : \mathbb{Z}^{m \times n \times 3} \rightarrow \mathbb{R}^{2L} : \mathbf{I}^{\text{raw}} \mapsto \mathbf{s}^{\text{raw}}, \quad (23)$$

to accurately predict the face shape \mathbf{s}^{raw} for an unmarked raw image \mathbf{I}^{raw} .

The raw dataset of marked truecolor images is first pre-processed before being used to devise a model for FLD. Preprocessing is important because working directly with the raw dataset makes the FLD task computationally more expensive. Moreover, the dataset of unconstrained truecolor images may vary largely in facial region size, face orientation, or illumination. Preprocessing of a raw image comprises three operations: image normalisation, feature extraction and feature selection [29, p. 2731]. The normalisation operation proceeds by first converting the raw images into grayscale images and detecting the facial region within each grayscale image by a face-detection algorithm such as the Viola–Jones algorithm [32]. The detected face region is then cropped and converted into a common-size image. We describe the normalisation process for each image by the map

$$\text{normalise} : \mathbb{Z}^{m \times n \times 3} \rightarrow \mathbb{Z}^{m_r \times n_r} : \mathbf{I}^{\text{raw}} \mapsto \mathbf{I}^{\text{norm}}, \quad (24)$$

where $m_r \times n_r$ is the size of grayscale images after normalisation and \mathbf{I}^{norm} denotes a normalised image. By normalisation, the face shape \mathbf{s}^{raw} of each raw image is scaled by the dimension (m_r, n_r) of the normalised image according to

$$\text{scale} : \mathbb{R}^{2L} \rightarrow \mathbb{R}^{2L} : \mathbf{s}^{\text{raw}} \mapsto \mathbf{s}, \quad (25)$$

where \mathbf{s} denotes the face shape of a normalised image. Thus, normalisation of marked images involves two functions, namely `normalise` and `scale`, acting on images and their corresponding landmarks, respectively.

³ In `OpenCV` [31], m and n denotes number of rows and columns of pixels, respectively.

⁴ In `OpenCV`, the coordinate system is an inverted Cartesian system with origin a the top-left corner. Each coordinate can be further bounded as $s_{i,2k}^{\text{raw}} \in [0, m]$ and $s_{i,2k+1}^{\text{raw}} \in [0, n]$

Feature extraction is performed by a feature descriptor

$$\text{extract} : \mathbb{Z}^{m_r \times n_r} \rightarrow \mathbb{R}^{F_{\text{norm}}} : \mathbf{I}^{\text{norm}} \mapsto \mathbf{x}^{\text{norm}}, \quad (26)$$

that maps a normalised image \mathbf{I}^{norm} into a feature vector \mathbf{x}^{norm} of size F_{norm} , which describes the normalised image. The common feature descriptors are the Haar-like feature descriptor [29] and the local binary patterns (LBP) feature descriptor [33]. To overcome the overfitting problem due to high dimensionality of feature vectors, F_{norm} is further reduced by feature selection techniques such as Adaboost regression [29] and correlation-based feature selection (CFS) [34]. A feature selection is a map

$$\text{select} : \mathbb{R}^{F_{\text{norm}}} \rightarrow \mathbb{R}^F : \mathbf{x}^{\text{norm}} \mapsto \mathbf{x}, \quad (27)$$

which maps a high-dimensional feature vector \mathbf{x}^{norm} of size F_{norm} to a low-dimensional feature vector \mathbf{x} of size F . We define all the operations in the preprocessing step as a composite function

$$\text{preprocess} = \text{select} \circ \text{extract} \circ \text{normalise}, \quad (28)$$

which maps a raw image \mathbf{I}^{raw} to a preprocessed feature vector \mathbf{x} .

The resultant dataset for a FLD problem after preprocessing the raw dataset (22) is

$$\mathcal{D} = \{(\mathbf{x}_i, \mathbf{y}_i) \mid i \in [N]\} \subset \mathbb{R}^F \times \mathbb{R}^{2L}. \quad (29)$$

Using this dataset, a model

$$\text{detect} : \mathbb{R}^F \rightarrow \mathbb{R}^{2L} : \mathbf{x} \mapsto \mathbf{s}, \quad (30)$$

is devised that maps the F -dimensional feature vector \mathbf{x} to the face shape \mathbf{s} of a normalised face image. The face shape of a raw face image is then achieved by `rescale`, which is defined as the inverse of `scale` (25) to \mathbf{s} . Finding a face shape is therefore the composition

$$\text{shape} = \text{rescale} \circ \text{detect} \circ \text{preprocess}, \quad (31)$$

which is the computational problem denoting a FLD task.

The literature shows a plethora of methods used to solve the FLD problem [13], with more recent and efficient algorithms developed by regression-based methods [21, 29]. These methods learn a regression model `detect` from the low-dimensional feature vector \mathbf{x} to the face shape \mathbf{s} of a normalised face image. Ref. [29] employs a method, termed “BoRMaN”, that combines SVR for local search and Markov random fields for global shape constraints, and yields fast and accurate detection of landmarks. We next cast FLD as a regression problem and describe a typical machine-learning workflow for solving the regression problem.

2. Landmark detection as a machine-learning problem

Here we describe a FLD problem as a machine-learning problem. First we cast FLD as a supervised-learning (SL) problem of multi-output regression. We then discuss a typical workflow for solving a SL problem. Finally, we elaborate on the individual steps of the workflow by describing the techniques relevant to our work.

The FLD problem is cast as a SL problem of multi-output regression [27]. The SL algorithm learns a model, using the dataset \mathcal{D} (29) that accurately predicts the face shape of a face image. This SL problem follows a typical machine-learning workflow, which involves four steps: data preprocessing, training, validation and testing.

We now describe all steps of the machine-learning workflow for FLD in detail. In the data preprocessing step, the raw dataset (22) is manipulated to construct a new dataset that is suitable for SL. This involves normalising the truecolor face images, feature extraction and feature selection as described in the previous section. For SL, the preprocessed dataset is divided into two disjoint sets as

$$\mathcal{D} = \mathcal{D}_{\text{model}} \sqcup \mathcal{D}_{\text{test}}, \quad (32)$$

where the size of $\mathcal{D}_{\text{model}}$ is M and size of $\mathcal{D}_{\text{test}}$ is $N - M$. The model dataset $\mathcal{D}_{\text{model}}$ is used for training and validating a model, and the test dataset $\mathcal{D}_{\text{test}}$ is used to test the model.

In the training step, the model dataset $\mathcal{D}_{\text{model}}$ is randomly divided into two disjoint data sets as

$$\mathcal{D}_{\text{model}} = \mathcal{D}_{\text{train}} \sqcup \mathcal{D}_{\text{validate}}, \quad (33)$$

for training set $\mathcal{D}_{\text{train}}$ of size T and validation set $\mathcal{D}_{\text{validate}}$ of size $V := M - T$. The training dataset is then used to construct a learning model

$$\widehat{\text{detect}} : \mathbb{R}^F \rightarrow \mathbb{R}^{2L} : \mathbf{x} \mapsto \tilde{\mathbf{s}}, \quad (34)$$

which is an approximation for the ideal model **detect** (30), and yields an approximate shape $\tilde{\mathbf{s}}$ of an unseen face image.

In the validation step, which sometimes is referred to as calibration [11], the constructed model in the training step is assessed by some performance measures, and hyperparameters of the model are then calibrated in an iterative way.

A cross-validation technique, such as Monte-Carlo cross-validation (MCCV) or k -fold cross validation [35], is commonly used for validating the constructed model. In this technique, a tuple of optimal hyperparameters of the model is obtained by searching over the hyperparameter space. For each tuple of hyperparameters, MCCV randomly samples a dataset $\mathcal{D}_{\text{train}}$, trains a model on it and calculates the model's performance on $\mathcal{D}_{\text{validate}}$, and repeat these steps for different pairs of $\mathcal{D}_{\text{train}}$ and $\mathcal{D}_{\text{validate}}$ to calculate a mean performance. After repeating this process for all possible tuples of hyperparameters,

the validation step returns the tuple corresponding to the best model performance.

In the testing step, performance of the learned model using the optimal hyperparameters is assessed on the test dataset $\mathcal{D}_{\text{test}}$, which is unseen in the training and validation steps. The model's performance in the testing step is reported as the final performance of the learned model. For comparing quality of different models for FLD, their performance on the same dataset are calculated using the standard metrics, as explained next.

3. Performance measures

We now discuss the standard datasets used for benchmarking a FLD model and commonly used performance measures for assessing the accuracy of a FLD algorithm.

The datasets used for testing a ML model for FLD include images of human faces along with manually labelled landmarks [13]. These datasets are constructed either under controlled conditions (constrained) or under uncontrolled conditions (unconstrained). Different datasets also vary in the total number of marked landmarks. Commonly used unconstrained datasets for FLD are BioID 2001 [36], Labeled Faces in the Wild 2007 (LFW) [37], Labeled Face Parts in the Wild 2011 (LFPW) [38] and Helen 2012 [39], whereas constrained datasets include IMM database [40] and PUT database [41].

Two performance measures are typically used to assess a FLD model's performance: mean normalised detection error (MNDE) and failure rate (FR) [21]. The detection error for each landmark is the Euclidean distance between the observed and the predicted coordinates. This error is normalised to make the performance measure independent of the actual face size or the camera zoom [42, p. 4]. Conventionally, the detection error is normalised by dividing with the inter-ocular distance, which is the Euclidean distance between the centre of the eyes [43]. However, this normalisation is biased for profile faces for which the inter-ocular distance can be very small [21, 44]. An alternative approach for normalisation, which does not have the drawback of the conventional normalisation, is dividing the detection error by the width of the face bounding box [21]. For each landmark k with the true coordinates (x_k, y_k) and the corresponding predicted coordinated $(\tilde{x}_k, \tilde{y}_k)$, the normalised detection error

$$e_k := \sqrt{(x_k - \tilde{x}_k)^2 + (y_k - \tilde{y}_k)^2} / d_k \quad (35)$$

where d_k is the inter-ocular distance or the width of the face bounding box. The MNDE for each landmark k over a dataset with N images is defined as the arithmetic mean of the normalised detection error for the landmark in each image of the dataset; that is

$$\text{MNDE}_k := \sum_{i=1}^N \frac{e_k^i}{N}, \quad (36)$$

where e_k^i is the normalised detection error for k th landmark of i th image.

To avoid biases of the MNDE, due to the variations in error normalisation, FR is also used as a measure for performance of a FLD model. For FR, a pre-specified thresholded value, denoted by e_{th} , is required for the normalised detection error (35). If the normalised detection error is greater than e_{th} then the detected landmark is considered as a failed detection. For each landmark k , the FR is defined as

$$\text{FR}_k := \frac{|\{i : e_k^i > e_{\text{th}}\}|}{N}, \quad (37)$$

which is the ratio of number of failed detection to the total number of images N ; the term ‘rate’ here refers to the ratio. The commonly used threshold value for failed detection is $e_{\text{th}} = 0.1$ [42, p. 4]. We use both MNDE and FR to gauge the accuracy of a FLD algorithm and to compare the performance of different FLD algorithms.

C. Quantum annealing on D-Wave

In this subsection, we briefly discuss the concept of quantum annealing and its practical realisation. First we explain quantum annealing as a meta-heuristic tool for optimisation. Then we state the equivalence between an Ising minimisation problem and a QUBO problem. Finally, we discuss D-Wave’s implementation of quantum annealing, with applications to SL.

1. Quantum annealing

Quantum annealing employs quantum-mechanical effects to approximate the solution of an optimisation problem, as we describe in the following. We start by defining the Ising minimisation problem and its relation to the computational problem of optimisation. We then define quantum annealing and explain how the process of quantum annealing results in finding the solution of a minimisation problem.

The computational problem of finding the global minimum is equivalent to the physical problem of finding the ground state of an Ising spin system, which is a collection of pairwise-interacting spin-1/2 particles in an external magnetic field. For a spin configuration $\{\sigma_i^Z\}$, h_i and J_{ij} represent the strength of the magnetic field on particle i and the coupling strength between adjacent particles i and j , respectively. The energy of this system is expressed by the Ising Hamiltonian

$$H_{\text{P}} := \sum_i h_i \sigma_i^Z + \sum_{\langle i,j \rangle} J_{ij} \sigma_i^Z \sigma_j^Z, \quad (38)$$

where the subscript ‘P’ denotes problem and the notation $\langle i, j \rangle$ denotes adjacency between particles i and j .

Here $\sigma_i^Z \in \{\pm 1\}$ for this classical H_{P} , whereas for a quantum particle, σ_i^Z represents the Pauli Z-matrix operating on particle i . Given coefficients $\{h_i\}$ and $\{J_{ij}\}$, the Ising minimisation problem is to find $\{\sigma_i^Z\}$ such that the system achieves the minimum or ground state energy.

Quantum annealing is a meta-heuristic optimisation procedure that aims to find the global minimum of a discrete optimisation problem using properties of quantum physics [8]. This optimisation problem is represented as an Ising minimisation problem by expressing the coefficients of the objective function in terms of $\{h_i\}$ and $\{J_{ij}\}$, and mapping the discrete variables to $\{\sigma_i^Z\}$. A classical analogue for quantum annealing is simulated annealing (SA), which is a numerical global optimisation technique with ‘‘temperature’’ guiding the simulated system towards a minimum energy state [45].

Quantum annealing relies on the adiabatic evolution of a time-dependent Hamiltonian [46]

$$H_{\text{QA}}(t/t_{\text{f}}) = -A(t/t_{\text{f}})H_{\text{I}} + B(t/t_{\text{f}})H_{\text{P}}, \quad (39)$$

for a duration t_{f} , which is called the annealing time. Ideally, the magnitude of t_{f} is determined from the difference between ground and first excited energy levels of $H_{\text{QA}}(t/t_{\text{f}})$ [46]. Here $A(t/t_{\text{f}})$ and $B(t/t_{\text{f}})$ are smooth and monotonic functions defining a preset annealing schedule, and the initial Hamiltonian H_{I} is a trivial Hamiltonian satisfying $[H_{\text{I}}, H_{\text{P}}] \neq 0$. At the beginning of an ideal quantum annealing process, the system starts in the ground state of H_{I} . For a transverse field Hamiltonian $H_{\text{I}} = \sum_i X_i$, its ground state is a uncoupled state, with each spin being in an equal superposition of $\sigma_i^Z = -1$ and $\sigma_i^Z = +1$. During annealing, the system Hamiltonian $H_{\text{QA}}(t/t_{\text{f}})$ slowly changes from H_{I} to H_{P} by decreasing $A(t/t_{\text{f}})$ smoothly from a maximum value to zero and increasing $B(t/t_{\text{f}})$ smoothly from zero to a maximum value. At the end of the anneal, the system is ideally in the ground state of H_{P} , which encodes the solution of the given discrete optimisation problem.

The Ising minimisation problem is equivalent to the computational problem of QUBO, under the linear transformation $s_i \mapsto 2a_i - 1$ [47]. A QUBO problem is finding the assignment of \mathbf{a} that minimises the objective function

$$E(\mathbf{a}) = \mathbf{a}^{\top} \tilde{\mathbf{Q}} \mathbf{a}, \quad a_i \in \{0, 1\}, \quad (40)$$

where \mathbf{a} is a column vector of the binary variables a_i and the QUBO matrix $\tilde{\mathbf{Q}}$ is a real-symmetric matrix. The diagonal and off-diagonal elements of $\tilde{\mathbf{Q}}$ can be expressed as functions of h_i and J_{ij} up to a constant. Additionally, the QUBO problem (40), or equivalently the Ising minimisation problem (38), can be represented as an undirected graph $G = \{V, E\}$. The set of nodes V corresponds to the spin-1/2 particles with $\{h_i\}$ and $\{J_{ij}\}$ corresponding to the weights of nodes and edges E , respectively.

2. D-Wave QA implementation

Now we proceed to describe D-Wave’s implementation of quantum annealing. First we explain the hardware and the cloud interface that we use. Finally, we provide some examples of D-Wave’s application to SL.

The D-Wave System Inc. offers a 5000-spin implementation of a practical quantum annealing device, commonly known as a quantum annealer or quantum processing unit (QPU). The spins in this annealer are superconducting flux qubits, operating at a temperature of 15 mK, which are arranged in a Pegasus topology [48]. The native connectivity of the annealer chip `Advantage_system` 1.1, which we use, has 5640 qubits (nodes) and 40484 couplers (edges), but a working chip typically has a fewer number of qubits and couplers due to technical imperfections. Although this restricted connectivity only allows complete graphs of size less than 180 to be solved directly on the annealer [49], using the quantum-classical hybrid annealing solver `hybrid_binary_quadratic_model_version2` [12] we can solve up to a 10^6 -variable optimisation problem.

D-Wave provides cloud-based access to its annealers using the quantum cloud service `Leap`. To make an optimisation problem compatible for a D-Wave solver, it needs to be first converted into an Ising minimisation problem (38) or a QUBO problem (40). Using predefined functions [50], the solver then embeds the problem into the Pegasus graph structure of the D-Wave annealer. The Hybrid Solvers employ state-of-the-art classical algorithms, aided with automatic intelligent access of the quantum annealer, to deliver the best solution for the optimisation problem. These solvers do not require precise manual controls of the annealers, making them suitable for various machine learning applications. However, we can choose the value of the parameter `time_limit`, which denotes the maximum allowed problem runtime [51].

D-Wave is utilised for a regression task on lattice quantum chromodynamics simulation data, where the D-Wave annealer performed comparably to the best classical regression algorithm [52]. D-Wave is used to train a linear regression model about thrice faster than the classical approach with similar values for regression error metric, when applied on a synthetic dataset [53]. Although no claims regarding a computational speedup over a classical soft-margin SVM is made, empirical evidence shows a better or comparable performance of quantum-annealing-based SVM in terms of classification accuracy, area under Receiver-Operating-Characteristic curve and area under Precision-Recall curve, for a dataset of size ≈ 1600 in a binary classification problem of computational biology [11].

III. APPROACH

In this section, we describe our approach for solving the regression problem of detecting facial landmarks us-

ing quantum-assisted ε -SVR models. We begin by explaining our method to construct a quantum-assisted ε -SVR model and to train it using a commercial quantum annealer. Then we describe our FLD algorithm, which involves converting the multi-output regression problem into several single-output regression problems and solving each of them using SVR. Finally, we elaborate on the machine-learning workflow for each of these single-output regression problems.

A. Quantum-assisted SVR

Here we explain our method for designing a quantum-assisted SVR, which involves employing quantum annealing for solving the dual formulation of the single-variable optimisation problem (14). First we show how to convert this optimisation problem into a QUBO problem (40). Then we describe implementations of two ε -SVR models, constructed by solving the QUBO problem using a classical or a quantum-classical hybrid algorithm. Finally, we briefly discuss the application of the quantum-assisted SVR formulation to the FLD problem, along with software packages utilised in this work.

Converting the optimisation problem in Eq. (14) into a QUBO problem (40) is a two-step procedure: first we convert the constrained optimisation into an unconstrained optimisation on real values, and then we convert the real-valued unconstrained optimisation into a binary form. To design an unconstrained optimisation problem, we construct a new objective function $\mathcal{L}(\boldsymbol{\alpha})$ by adding the first constraint in Eq. (14b) as a square-penalty term to the objective function (14a) using a Lagrange multiplier $\lambda \in \mathbb{R}^+$ [54]. The solution of the unconstrained optimisation problem is a vector $\boldsymbol{\alpha} \in \mathbb{R}^{2M}$. For each element of $\boldsymbol{\alpha}$, we define a binary encoding [11], with total number of bits B and with B_f bits representing the fractional part, as

$$\alpha_m \approx \frac{1}{2^{B_f}} \sum_{i=0}^{B-1} 2^i a_{Bm+i} \quad \forall m \in [2M], \quad (41)$$

up to the encoding precision 2^{-B_f-1} . By this encoding, we obtain an objective function $E(\mathbf{a})$, which is in the QUBO form (40). Additionally, with the choice for the regularization hyperparameter

$$\gamma \approx \frac{1}{2^{B_f}} \sum_{i=0}^{B-1} 2^i = \frac{1}{2^{B_f}} (2^B - 1), \quad (42)$$

which, up to the encoding precision, is the maximum value possible for each α_m , the second constraint in Eq. (14b) is also satisfied.

We employ two different algorithms to solve the constructed QUBO problem, i.e., to minimise the objective function $E(\mathbf{a})$ (40), and compare their performances. One of the algorithms is purely classical and the other is a hybrid quantum-classical algorithm. We choose SA

for classical optimisation and D-Wave’s Hybrid Solver for quantum-classical hybrid optimisation, as SA and Hybrid are the typical choices in this field [25, 26]. For SA, we use the implementation in D-Wave’s package `dwave-neal` [55], and use `LeapHybridSampler` [12] for hybrid optimisation. The output of each algorithm is a binary vector \mathbf{a} , which after decoding by Eq. (41) yields the solution $\boldsymbol{\alpha}$ of the unconstrained optimisation problem in Eq. (14). Having $\boldsymbol{\alpha}$, we compute the offset b (17) by the method described in Appendix A. The vector $\boldsymbol{\alpha}$ together with the offset b are then used to construct an ε -SVR model (17), where ε is the error tolerance in Eq. (3). Henceforth, we refer to the ε -SVR models constructed by SA and Hybrid (quantum-assisted) solver as “SA-SVR” and “QA-SVR”, respectively.

We apply this quantum-assisted ε -SVR formulation to the computational problem in FLD. In the following subsections, we describe our approach for using QA-SVR and SA-SVR, and compare their performances for the FLD task (23). We also compare these models against the standard ε -SVR model, which we refer to as “SKL-SVR”, constructed using Python’s `scikit-learn` [28] and is based on gradient-based optimisation [24].

B. Algorithm for FLD

In this subsection, we explain our procedure for constructing and benchmarking SL models to solve the FLD task (23). First we describe the raw datasets used for training, validating and testing. Then we decompose the FLD task into independent sub-tasks and state the SL problem, along with the preferred SL model, for each sub-task. Finally, we elaborate on the assessment procedure for a landmark-detection model.

1. Raw datasets

We begin by describing the raw datasets used in our work. First we elucidate the structure of the datasets, i.e., what information is contained in them, along with an example face image. Finally, we state our convention for choosing the training and test datasets.

We use the datasets compiled from the publicly available databases LFW, LFPW and BioID for training, validating and testing our SVR models [21, 56]. The raw dataset \mathcal{D}^{raw} (22), with $N = 125$ images and $L = 5$ landmarks, is a subset of the LFW image database. Each face shape is represented by a list of (x, y) coordinates⁵ of five facial landmarks: left-eye centre (1), right-eye centre (2),

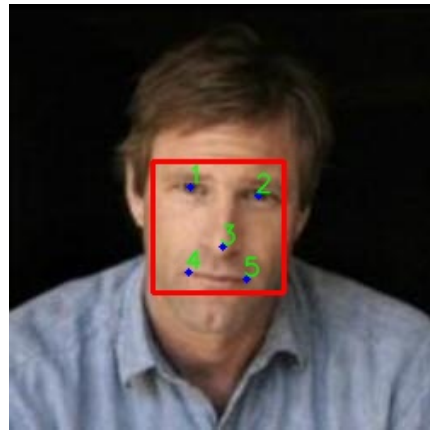


FIG. 2. An example image from the LFW database [37]. Using data from Ref. [56], we show the five landmarks with manually determined positions, labels 1–5, and the face box as a red rectangle.

nose tip (3), left mouth corner (4) and right mouth corner (5); see Fig. 2. In addition to the face shape, \mathcal{D}^{raw} includes a representation of the face box, shown in Fig. 2, which demarcates the extent of the face. A face box is defined by a list of four numbers: first and third numbers are the coordinates of the top-left corner of the box, and the second and fourth numbers are the coordinates of the bottom-right corner. Although these coordinates can vary depending on the face detection algorithm and can have biases based on age, gender, race, etc., in this paper we just use the pre-determined data [56].

From \mathcal{D}^{raw} , we randomly choose a subset $\mathcal{D}_{\text{model}}^{\text{raw}}$ of size 100 for training and validation, and the remaining 25 datapoints make the test set $\mathcal{D}_{\text{test}}^{\text{raw}}$. To evaluate our FLD algorithm and compare its performance with the state-of-the-art SVR-based FLD algorithm [29], we test our learned models over subsets of two benchmarking databases for FLD, namely LFPW and BioID. These two are the commonly used databases for unconstrained images, with BioID having lesser variations in face pose, illumination and expression as compared to LFPW. From these two databases, we choose subsets of sizes 164 and 1341, respectively, as our test datasets.

2. Landmark-detection model

We now elaborate on our FLD algorithm for constructing a landmark-detection model, and our procedure to assess and compare this model against state-of-the-art model. For images with L landmarks, we first split the FLD task (23) into $2L$ sub-tasks, where each sub-task is to solve a single-output regression problem. We then construct an ε -SVR model (17) for solving this problem. Next we obtain a landmark-detection model using models for the x and y coordinates of all landmarks. Finally, we elaborate on our choice of performance metrics and test datasets used for benchmarking.

⁵ Here the coordinate system is an inverted Cartesian system with the origin at the top-left corner of the image. This inverted coordinate system is the same as in `OpenCV` where images are represented as matrices.

We design a FLD algorithm that solves the FLD task (23) by splitting into $2L$ independent sub-tasks labelled by $\ell \in [2L]$. The raw dataset for sub-task ℓ

$$\mathcal{D}_\ell^{\text{raw}} = \{(\mathbf{I}_i^{\text{raw}}, s_{i,\ell}^{\text{raw}}) \mid i \in [N]\} \subset \mathbb{Z}^{m \times n \times 3} \times \mathbb{R}, \quad (43)$$

is a subset of \mathcal{D}^{raw} (22). Given the above dataset, the sub-task is then to devise a model

$$\text{shape}_\ell : \mathbb{Z}^{m \times n \times 3} \rightarrow \mathbb{R} : \mathbf{I}^{\text{raw}} \mapsto s_\ell^{\text{raw}} \quad (44)$$

that accurately predicts s_ℓ^{raw} for an unmarked raw image \mathbf{I}^{raw} . By concatenating outputs of these $2L$ models (44), we obtain the face shape \mathbf{s}^{raw} (21) of \mathbf{I}^{raw} . Thus solving the $2L$ sub-tasks solves the FLD task of predicting the face shape.

Each sub-task ℓ (44) involves a nonlinear single-output regression problem, which we solve by employing machine learning. Using a dataset $\mathcal{D}^{(\ell)}$, generated from $\mathcal{D}_\ell^{\text{raw}}$ (43) by preprocessing operations, the SL agent learns a regression model $\widehat{\text{detect}}_\ell$. This model predicts the scaled value of one coordinate of one landmark, as explained thoroughly in the next section. Due to the nonlinearity property and the high-generalisation capability of SVR [29], we represent each $\widehat{\text{detect}}_\ell$ by an ε -SVR model (17) with Gaussian kernel (19). Moreover, we compare between classical and quantum-assisted algorithms by constructing three different ε -SVR models, namely QA-SVR, SA-SVR and SKL-SVR, for each $\widehat{\text{detect}}_\ell$.

We now construct a landmark-detection model by combining the detection models for x and y components of each landmark. The landmark-detection model for the k th landmark is

$$\widehat{\text{landmark}}_k = (\widehat{\text{shape}}_{2k}, \widehat{\text{shape}}_{2k+1}), \quad (45)$$

where $\widehat{\text{shape}}_{2k}$ and $\widehat{\text{shape}}_{2k+1}$ approximately predict the x and y components of landmark k , respectively. Each $\widehat{\text{shape}}_{2k}$ is constructed using the corresponding $\widehat{\text{detect}}_{2k}$, which in turn has three formulations based on the nature of algorithm, i.e. QA-SVR, SA-SVR and SKL-SVR. Consequently, a landmark-detection model, which is a collection $(\widehat{\text{landmark}}_k, \forall k \in [L])$, is of three types: QA-landmark, SA-landmark and SKL-landmark.

To evaluate the efficacy of a landmark-detection model, we use the mean and variance of normalised detection error and the failure rate, calculated for all L landmarks. The output of each $\widehat{\text{landmark}}_k$ is a tuple (\hat{x}_k, \hat{y}_k) , which are the predicted values for the x and y coordinates of the landmark relative to the top-left corner of the image. Using these predicted coordinates, the true coordinates (x_k, y_k) and the width of the face bounding box as d_k , we calculate MNDE_k (36) and the variance of e_k (35). We also calculate FR_k (37) for a threshold $e_{\text{th}} = 0.1$.

We test and compare four landmark-detection models on three benchmarking datasets. Three of these models, i.e. QA-landmark, SA-landmark and SKL-landmark, are trained using our FLD algorithm, whereas the fourth

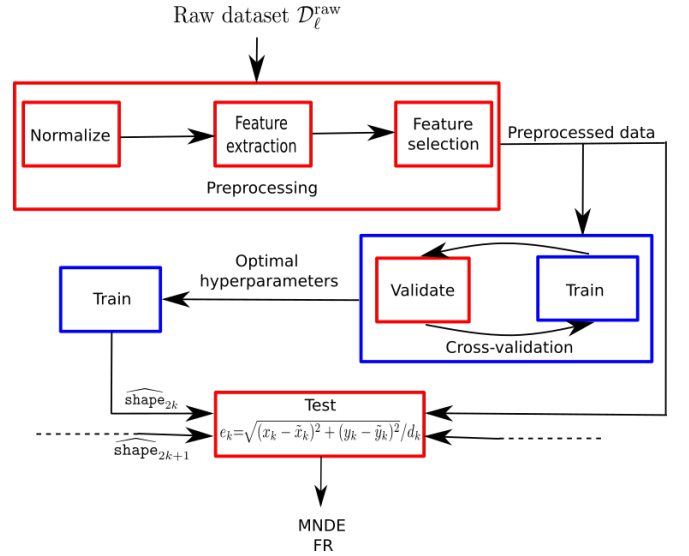


FIG. 3. ML workflow for constructing and characterising a landmark-detection model. The red boxes represent purely classical operations. Each blue box denotes an operation that can be either classical, quantum or a hybrid of both.

model is trained using the state-of-the-art classical FLD algorithm based on boosted-SVR [29]. Each of these four models is assessed by metrics MNDE, variance of detection error and FR, calculated using subsets of the standard databases, i.e. LFW, LFPW and BioID [56].

C. Machine learning workflow

Here we elaborate on the machine learning workflow [Fig. 3] for devising a model $\widehat{\text{shape}}_\ell$, which approximates the desired model (44) for a sub-task ℓ . We begin by describing the preprocessing operations that are applied on the raw dataset to generate a processed dataset. Using this processed dataset, we then construct an ε -SVR model, which approximately predicts one coordinate of one landmark for a normalised image. In this regard, we explain optimal hyperparameter selection, training and testing for this model.

1. Preprocessing raw dataset

We elaborate on the first step of the workflow, i.e. preprocessing the raw dataset $\mathcal{D}_\ell^{\text{raw}}$ (43). Preprocessing typically involves three sub-steps, namely normalisation (24,25), feature extraction (26) and feature selection (27). We provide implementation details of these three sub-steps. Finally, we derive the pre-processed dataset $\mathcal{D}^{(\ell)}$, which is later used for training an ε -SVR model (17).

The raw dataset $\mathcal{D}_\ell^{\text{raw}}$ comprises 125 LFW images of varying facial-region size, orientation and illumination,

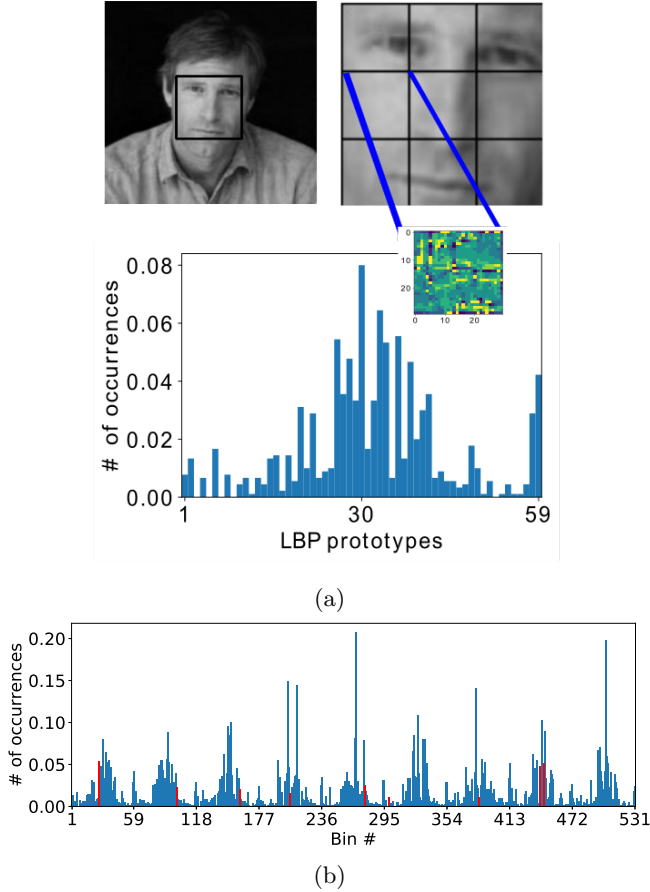


FIG. 4. Pictorial depiction of the preprocessing step. (a) Top two figures highlight the essential components of normalisation: first is the 2D grayscale image with the face detection box and second is the cropped and resized image. Top second figure and bottom figure together depict the essentials of feature extraction: we show 3×3 image segments, along with non rotation-invariant uniform LBP for one segment, and the 59-dimensional normalised histogram representation for this LBP. (b) Feature extraction and selection: spatially-enhanced histogram, generated by concatenating the nine LBP histograms, represents a 531-dimensional feature vector. The sparse red bars represent the low-dimensional feature vector after feature selection.

and hence this dataset needs to be normalised before being used for training ε -SVR models. To normalise these images according to `normalise` (24), we first convert each truecolor face image into its gray-scale version using a pre-defined function [57] of the `OpenCV` package. Next we crop the facial region of each gray-scale image by extracting the sub-matrix corresponding to the coordinates (integer part) in the face box. Finally, each cropped image is resized to 90×90 ($m_r = n_r = 90$ in Eq. (24)), which is an approximate average of the dimensions of 125 images, using `OpenCV`'s `resize` function [58]. Additionally, for each normalised image \mathbf{I}^{norm} , the scaled

coordinate $s^{(\ell)}$ is calculated using

$$\text{scale}_\ell : \mathbb{R} \rightarrow \mathbb{R} : s_\ell^{\text{raw}} \mapsto s^{(\ell)}, \quad (46)$$

from the actual coordinate s_ℓ^{raw} (43).

We now apply the feature extraction `extract` (26) on each 90×90 image \mathbf{I}^{norm} to construct the corresponding feature vector \mathbf{x}^{norm} . To this end, we choose LBP as our image descriptor because local descriptors are robust with respect to pose and illumination changes in images and are invariant to hyperparameter selection [59]. We divide \mathbf{I}^{norm} into a 3×3 grid of equal segments and calculate the LBP histogram for each segment using the LBP implementation of Python's `scikit-image` package [60]; see Fig. 4(a). Upon choosing a circular (8,1) neighbourhood and restricting LBPs to only non-rotation-invariant uniform patterns, the LBP histogram for each segment has 59 bins, where 58 bins hold frequencies of 58 uniform patterns and all non-uniform patterns are counted in the remaining bin [61]. We use the spatially-enhanced histogram representation [59], which is the concatenation of the nine LBP histograms corresponding to the nine segments, as a 531-dimensional feature vector \mathbf{x}^{norm} . In Fig. 4(b), we represent this spatially enhanced histogram as an extended histogram plot with 531 bins.

In the final sub-step of preprocessing, i.e., feature selection, we use the CFS technique. The correlations between the feature vectors $\{\mathbf{x}_i^{\text{norm}}\}$ (26) and corresponding outputs $\{s_i^{(\ell)}\}$ (46) is quantified by their Pearson correlation coefficients. By this Pearson CFS technique, we then reduce the 531-dimensional vector \mathbf{x}^{norm} to a F_ℓ -dimensional vector $\mathbf{x}^{(\ell)}$ according to

$$\text{select}_\ell : \mathbb{R}^{531} \rightarrow \mathbb{R}^{F_\ell} : \mathbf{x}^{\text{norm}} \mapsto \mathbf{x}^{(\ell)}, \quad (47)$$

where $F_\ell < 10$. This bound for F_ℓ is chosen to avoid overfitting during training with 10 data points in the MCCV step, as explained later in this section. The Pearson coefficients are calculated using a pre-defined function `pearsonr` of Python's `scipy` package [62]. The selected features in the 531-dimensional vector are represented as red bars in the concatenated histogram; see Fig. 4(b).

Performing the three image preprocessing operations (24,26,47) on each raw face image and the scaling operation (46) on the corresponding landmark coordinate, we derive the preprocessed dataset $\mathcal{D}^{(\ell)}$ from the raw dataset $\mathcal{D}_\ell^{\text{raw}}$ (43). The three operations (24,26,47) can be combined as a function

$$\text{preprocess}_\ell = \text{select}_\ell \circ \text{extract} \circ \text{normalise}, \quad (48)$$

which maps \mathbf{I}^{raw} to $\mathbf{x}^{(\ell)}$. Thus, using `preprocess` _{ℓ} and `scale` _{ℓ} , we generate

$$\mathcal{D}^{(\ell)} = \left\{ \left(\mathbf{x}_i^{(\ell)}, s_i^{(\ell)} \right) \mid i \in [N] \right\} \subset \mathbb{R}^{F_\ell} \times \mathbb{R}. \quad (49)$$

Furthermore, this dataset is an union (32) of two disjoint sets,

$$\mathcal{D}^{(\ell)} = \mathcal{D}_{\text{model}}^{(\ell)} \sqcup \mathcal{D}_{\text{test}}^{(\ell)}, \quad (50)$$

where $\mathcal{D}_{\text{model}}^{(\ell)}$ and $\mathcal{D}_{\text{test}}^{(\ell)}$ are obtained from $\mathcal{D}_{\text{model}}^{\text{raw}}$ and $\mathcal{D}_{\text{test}}^{\text{raw}}$, respectively, for each sub-task ℓ by employing the two preprocessing functions (46,48).

2. Training and testing?

We now explain the procedure to train, validate and test an ε -SVR model using the dataset $\mathcal{D}^{(\ell)}$ (50). First we discuss implementation of the training step in our workflow. Next we define the hyperparameter subsets for the ε -SVR model, followed by a discussion on our MCCV implementation. Finally, we construct the ε -SVR model, which is then used for testing our algorithm.

We use the preprocessed dataset $\mathcal{D}_{\text{model}}^{(\ell)}$ for training an ε -SVR model. Using a randomly chosen subset $\mathcal{D}_{\text{train}}^{(\ell)}$ from $\mathcal{D}_{\text{model}}^{(\ell)}$, we construct the model

$$\widehat{\text{detect}}_{\ell} : \mathbb{R}^{F_{\ell}} \rightarrow \mathbb{R} : \mathbf{x}^{(\ell)} \mapsto \tilde{s}^{(\ell)}, \quad (51)$$

which approximately predicts the value of $s^{(\ell)}$ (46) as $\tilde{s}^{(\ell)}$. In order to compare classical vs hybrid algorithms, we generate three different $\widehat{\text{detect}}_{\ell}$ models, namely SKL-SVR, SA-SVR and QA-SVR. We fix the error tolerance as $\varepsilon = 0.1$, which is the default value in LIBSVM [63] and its implementation in `scikit-learn` [28], for all these three models. For the SA solver, we fix both the number of sweeps and the number of repetitions to 1000, and use the iteratively-averaged value over 20 low-energy samples as the solution for the QUBO problem [10]. For the Hybrid Solver, we fix the parameter `time.limit` to 3s and 6s for cross-validation and training, respectively, where these values are selected according to the number of variables in the QUBO problem [64]. Furthermore, we report the average prediction over 20 models as the value of $\tilde{s}^{(\ell)}$ to account for the probabilistic nature of the SA and Hybrid Solvers [11].

Now we determine hyperparameter domains for each of the three ε -SVR models, namely SKL-SVR, SA-SVR and QA-SVR. We restrict the domain of each hyperparameter to a small subset based on certain assumptions and our observations. We fix $B_f = 0$ (41), which is justified because fractional part was not required for getting feasible solutions from classification models built using SVMs [11]. Consequently, γ (42) can only be certain integer values. We pick $\gamma \in \{15, 31, 63\}$, corresponding to $B \in \{4, 5, 6\}$. These bounds are justified empirically by observing insignificant changes in solutions for QUBOs with γ outside this range. We estimate the default value for the Gaussian kernel parameter (20) as $\eta = 238$ using feature dimension $F_{\ell} = 6$ (on average) and variance of training dataset as 0.0007 (on average). Assuming $\eta = 238$ as the upper bound, we choose $\eta \in \{4, 4^2, 4^3, 4^4\}$, which exponentially covers the domain for η and is enough for our problem. Furthermore, for the Lagrange multiplier λ , we empirically choose a feasible subset $\{1, 5, 10\}$ as its domain. In summary, for

SKL-SVR, the domain for each hyperparameter in the tuple (γ, η) is

$$\gamma \in \{15, 31, 63\}, \eta \in \{4, 4^2, 4^3, 4^4\}, \quad (52)$$

and for SA-SVR and QA-SVR, the hyperparameter tuple is (B, B_f, η, λ) , with their corresponding domains

$$\begin{aligned} B &\in \{4, 5, 6\}, B_f = 0, \\ \eta &\in \{4, 4^2, 4^3, 4^4\}, \lambda \in \{1, 5, 10\}. \end{aligned} \quad (53)$$

In the validation step, we use the MCCV technique to find the optimal tuple of hyperparameters for an ε -SVR model (17). Our MCCV works as follows. By randomly sampling 10% of $\mathcal{D}_{\text{model}}^{(\ell)}$, without replacement, generate a dataset $\mathcal{D}_{\text{train}}^{(\ell)}$. Then train a model using $\mathcal{D}_{\text{train}}^{(\ell)}$ and validate on $\mathcal{D}_{\text{validate}}^{(\ell)}$, which is the remaining 90% of $\mathcal{D}_{\text{model}}^{(\ell)}$. We repeat this process 50 times for each tuple of hyperparameters, i.e. (γ, η) for SKL-SVR and (B, B_f, η, λ) for SA-SVR and QA-SVR, and finally choose the one tuple returning the minimum value of a performance metric called mean normalised error (MNE), which is similar to MNDE (36). We define MNE for each coordinate of each landmark as

$$\text{MNE}^{(\ell)} := \frac{1}{V} \sum_{m=1}^V \frac{s_m^{(\ell)} - \tilde{s}_m^{(\ell)}}{90}, \quad (54)$$

where $V = 90$ is size of our validation dataset. From this MCCV step, we calculate the optimal tuple of hyperparameter and use it in the final training step.

We construct the final ε -SVR model $\widehat{\text{detect}}_{\ell}$ (51) using the whole dataset $\mathcal{D}_{\text{model}}^{(\ell)}$ and the best hyperparameter tuple from MCCV. The sub-task in Eq. (44) is then approximately accomplished by following the composition

$$\widehat{\text{shape}}_{\ell} = \text{rescale}_{\ell} \circ \widehat{\text{detect}}_{\ell} \circ \text{preprocess}_{\ell}, \quad (55)$$

where rescale_{ℓ} is the inverse of scale_{ℓ} (46). The function $\widehat{\text{shape}}_{\ell}$ yields an approximate prediction $\tilde{s}_{\ell}^{\text{raw}}$ of one coordinate of one landmark for each image in $\mathcal{D}_{\text{test}}^{(\ell)}$. This prediction, along with the prediction for the other coordinate [Fig. 3], are then used to construct and assess the landmark-detection model (45).

IV. RESULTS

In this section, we present our results on the performance of our quantum-assisted algorithm for FLD and compare our algorithm with classical algorithms for FLD. First we formulate the optimisation problem involved in training an ε -SVR model as a QUBO problem. Then we compare the performances of the three landmark-detection models developed here, namely `SKL-landmark`, `SA-landmark` and `QA-landmark`, using a subset of the LFW dataset. Finally, using the LFPW and BioID datasets, we compare these landmark-detection models against a model constructed by the BoRMaN algorithm.

A. QUBO formulation of SVR

Here we construct a QUBO formulation for the constrained optimisation problem (14) used in training an ε -SVR model. We begin by deriving a real-valued unconstrained optimisation problem corresponding to the constrained optimisation problem. Then we establish an expression for the QUBO matrix, which is used to derive the QUBO objective function $E(\mathbf{a})$ (40).

For the real-valued unconstrained optimisation problem, we derive the objective function $\mathcal{L}(\boldsymbol{\alpha})$ by adding the first constraint in Eq. (14b) as a square-penalty term to the objective function (14a) using the Lagrange multiplier λ . We obtain the expression

$$\mathcal{L}(\boldsymbol{\alpha}) := \frac{1}{2} \boldsymbol{\alpha}^\top \mathbf{Q} \boldsymbol{\alpha} + \boldsymbol{\alpha} \cdot \mathbf{c} + \lambda \left(\sum_{m=0}^{M-1} \alpha_m - \sum_{m=M}^{2M-1} \alpha_m \right)^2, \quad (56)$$

for this real-valued objective function. The solution of this unconstrained optimisation problem is the vector $\boldsymbol{\alpha} \in \mathbb{R}^{2M}$ that minimises $\mathcal{L}(\boldsymbol{\alpha})$ and satisfies the bounds imposed by the second constraint in Eq. (14b).

We now express the objective function (56) of the unconstrained optimisation problem in a QUBO form (40). By employing the binary encoding (41), we derive the $2MB \times 2MB$ symmetric QUBO matrix $\tilde{\mathbf{Q}}$, with elements

$$\begin{aligned} \tilde{Q}_{Bn+i, Bm+j} = & \frac{1}{2} \frac{2^{i+j}}{2^{2B_f}} Q_{nm} + \frac{2^i}{2^{B_f}} \delta_{nm} \delta_{ij} c_n + \lambda \frac{2^{i+j}}{2^{2B_f}} \\ & - 2\lambda \frac{2^{i+j}}{2^{2B_f}} \bar{\Theta}(m-M) \Theta(n-M) \\ & - 2\lambda \frac{2^{i+j}}{2^{2B_f}} \bar{\Theta}(n-M) \Theta(m-M), \end{aligned} \quad (57)$$

where

$$\Theta(n) := \begin{cases} 0 & \text{if } n < 0, \\ 1 & \text{if } n \geq 0, \end{cases} \quad (58)$$

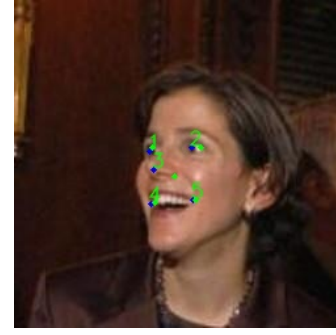
is the Heaviside step function and

$$\bar{\Theta}(n) := 1 - \Theta(n) \quad \forall n \in \mathbb{Z}. \quad (59)$$

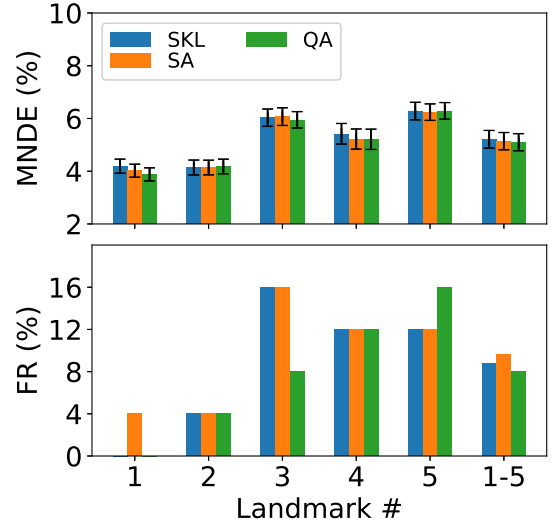
The QUBO matrix is then used to express the optimisation problem in the QUBO form as

$$E(\mathbf{a}) = \sum_{n,m=0}^{2M-1} \sum_{i,j=0}^{B-1} a_{Bn+i} \tilde{Q}_{Bn+i, Bm+j} a_{Bm+j}, \quad (60)$$

see Appendix B for a detailed derivation of this QUBO problem. Minimising $E(\mathbf{a})$ (60) produces a $(2MB)$ -bit string \mathbf{a} , which upon decoding consistent with Eq. (41), yields an approximate solution of the unconstrained optimisation problem (14), up to the encoding precision.



(a)



(b)

FIG. 5. Performance of our FLD algorithm on a subset of the LFW test dataset consisting of 25 facial images. (a) Predictions from QA-landmark model: actual landmark positions (in blue) and predicted landmark positions (in green) for a LFW test image; (b) Comparison between the three models, namely SKL-landmark, SA-landmark and QA-landmark for 25 LFW images: for each of the five landmarks and their aggregate, we show MNDE (in %) and FR (in %) as barplots, and the error bar for MNDE corresponds to the standard deviation over detection errors.

B. Quantum-assisted facial-landmark detection

We characterise the three implementations of our landmark-detection model (45), namely SKL-landmark, SA-landmark and QA-landmark. Each of these three models is trained and tested using subsets of the LFW database [21, 56]. We begin by comparing the true and predicted positions of five landmarks on a LFW test image. Then we compare the three landmark-detection models based on their mean (36) and variance of normalised detection errors (35) for each of the five landmarks and their aggregate. Finally, we present results for FR (37) of the three models.

We show detection results of the QA-landmark model for a test image from the LFW test dataset in Fig. 5(a).

To assess the efficacy of our trained landmark-detection model, we select an unconstrained LFW image, which has a non-frontal face with expression. For the selected test image, the predicted positions of four landmarks (#1, #2, #4, #5) overlap with their corresponding true positions. The predicted coordinates for landmark #3, i.e., tip of the nose, agree less to the actual coordinates by a normalised error (35) of 19%.

In Fig. 5(b), we compare the statistics of detection errors for the three landmark-detection models over a randomly selected subset of the LFW test dataset, comprising 25 manually marked facial images. QA-landmark delivers marginally lower MNDE than the two classical models for landmarks #1, #3 and #4, but within the error bars. For the aggregate case, i.e. the union of detection errors for all five landmarks, all three models are equivalent in terms of the mean and variance of detection errors. Quantitatively, MNDE for QA-landmark is 1% and 2% less than the MNDEs for SA-landmark and SKL-landmark, respectively. Moreover, the variance of detection errors for the QA-landmark model is 2% (7%) less than that for SA-landmark (SKL-landmark) model.

Figure 5(b) shows the FR (37) for each of the five landmarks and for the aggregate case, calculated using each of the three landmark-detection models. For landmark #1, the SKL-landmark and QA-landmark models yield zero for the failure rate, signifying that detection errors never exceed the threshold $e_{th} = 0.1$ for any image in our test dataset. The QA-landmark model for landmark #3 is significantly more successful than both classical detection models. For the aggregate case, FR of QA-landmark is 20% and 10% less than the FRs for SA-landmark and for SKL-landmark, respectively.

C. Benchmarking

We now present our results on the comparison between four FLD models, namely SKL-landmark, SA-landmark, QA-landmark and the model constructed by the BoRMaN algorithm [29]. Our comparison is based on assessing the efficacies of these models for the benchmarking datasets constructed from the LFPW and BioID databases [21, 56].

Using the LFPW dataset, we calculate and plot means and variances of detection errors, and FRs for five landmarks and their aggregate [Fig. 6(a)]. The model constructed by the BoRMaN algorithm delivers an aggregate MNDE about 18% less than that of the QA-landmark model, which within error bars is similar to the SA-landmark and SKL-landmark models. In terms of FR (37), the BoRMaN model is slightly ($\approx 10\%$) better than the other three models. All three implementations of our FLD algorithm result in a variance of 0.135, which is about half of the variance resulted by the BoRMaN model.

We now compare results for the four models applied to the BioID dataset, shown in Fig. 6(b). Similar to

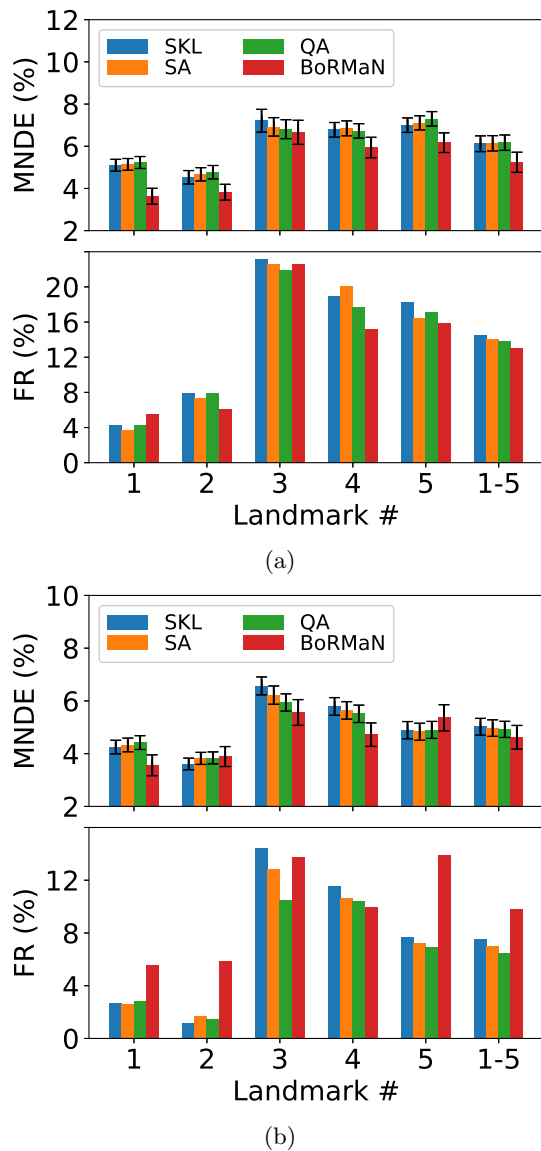


FIG. 6. Performance comparison between the three FLD models generated by our algorithm, namely SKL-landmark, SA-landmark and QA-landmark, and the model generated by the BoRMaN algorithm for two test datasets: LFPW and BioID. Similar to Fig. 5(b), MNDE and FR are represented by bar plots, and standard deviation of detection errors is represented by the error bar on MNDE. (a) The test dataset comprises 164 LFPW images; (b) The test dataset comprises 1341 BioID images.

the results for LFW and LFPW datasets, QA-landmark is slightly ($< 20\%$) better than SA-landmark and SKL-landmark over all five landmarks. The QA-landmark is superior to the classical model constructed using BoRMaN algorithm by about 50% and 100% in the estimates of FR and detection-error variance, respectively. Compared to our models, the BoRMaN model yields a lower (6%) aggregate MNDE.

V. DISCUSSION

In this section, we discuss the results of implementing our quantum-assisted algorithm for detecting facial landmarks on a practical quantum annealer. We begin by analysing the derived unconstrained formulation for the optimisation problem involved in generating an ε -SVR model. Then we elaborate on the quantum-classical hybrid implementation of our algorithm. Finally, we inspect and compare the performance of our algorithm against a state-of-the-art algorithm for FLD.

We construct a quantum-assisted ε -SVR model using D-Wave’s quantum annealer. For the purpose of generating this model, we cast the constrained optimisation problem (14) into a QUBO problem (40) by first deriving an unconstrained optimisation problem and then expressing this optimisation problem over binary variables. The derived QUBO objective function (60) is equivalent to the original objective function (14a) up to a judicious choice of the Lagrange multiplier λ and the encoding parameters (41). Due to imprecision of this real-to-binary encoding, our ε -SVR formulation is approximate.

We train the quantum-assisted ε -SVR model using D-Wave’s Hybrid Solver, which uses a combination of classical algorithms and quantum annealing for optimising a QUBO problem. Due to restrictions on the number and connectivity of qubits on a D-Wave QPU, the size of a fully connected graph that can be directly embedded onto the hardware is 180 for the 5000-qubit chip. This limitation has led to the use of batch learning approaches for previous machine learning tasks on D-Wave annealers [10, 11]. In this work, we thus make use of the Hybrid Solver for SL, which has two benefits: solving QUBO problems with a million variables and bypassing the QPU’s hyperparameter optimisation requirement. Additionally, we observe that training ε -SVR models using Hybrid Solver is easier, faster and results in better performance than using a limited-size QPU.

We employ the quantum-assisted ε -SVR model for efficient detection of facial landmarks, and assess its efficacy relative to both classical implementations, i.e., SA and `scikit-learn`, of our FLD algorithm. Following the standard 80:20 rule in machine learning, we perform training and testing of these models using 100 and 25 LFW images, respectively. On applying the quantum-assisted landmark-detection model on an example LFW test image, we observe that the predicted positions of four landmarks, namely eyes and mouth corners, are in good agreement with their corresponding true values, whereas the detection of the nose tip failed according to the standard failure threshold [42]. We observe that over all the 25 test images, these three models show, on average, equivalent efficacy within statistical variations. Although we observe a slight advantage of the quantum-assisted model, we interpret this advantage as a statistical fluctuation and not a quantum advantage, as is claimed for similar works [10, 11].

We compare the three implementations of our FLD al-

gorithm with the BoRMaN algorithm [29], which is state-of-the-art in SVR-based algorithms for FLD. In our algorithm, the ε -SVR models are trained using a smaller dataset, which is about one-quarter of the dataset used in BoRMaN, and all these four implementations are consequently tested on the benchmarking datasets of LFPW and BioID [56]. For each of these two test datasets, the average prediction error-rate obtained by using the BoRMaN algorithm slightly exceeds the rate obtained from our FLD algorithm, which contrarily has significantly lower variance as compared to that of the BoRMaN algorithm. In particular, the annealing-based implementations generate more accurate ε -SVR models with lower variances as compared to `scikit-learn` and BoRMaN. We contribute this advantage to the fact that annealing-based methods employ global optimisation of the Lagrange function (9), as compared to a greedy approach of `scikit-learn` and BoRMaN. Additionally, the SVR model generated using SA or Hybrid is an average of 20 feasible models, which in turn reduces the variance of MNDE for the test dataset.

VI. CONCLUSIONS

We have adapted SVR, a popular tool in supervised learning, into a quantum-assisted formulation. Our formulation employs quantum annealing for solving the optimisation problem, which is used to train the SVR model, with high accuracy. We have constructed a quantum-assisted SVR model using D-Wave’s Hybrid Solver and utilised this model for detecting five facial landmarks: centres of both eyes, tip of the nose and corners of the mouth. Furthermore, we tested efficacy by comparing landmark predictions of this model to predictions obtained from three classical models.

We have chosen the problem of FLD because it plays a key role in face recognition by assisting the conversion of unconstrained images to constrained images. Recent FLD algorithms, which are based on neural networks and regression techniques, yield the best detection accuracies so far. However, the success of these algorithms depends on the quality of available training datasets and the available computational power. As training an efficient and robust FLD model using a finite dataset of unconstrained images is still challenging for classical FLD algorithms, exploring quantum-assisted alternatives is thus worthwhile.

Quantum-assisted algorithms based on quantum annealing are shown to be empirically advantageous over classical algorithms for a variety of machine-learning problems. Notable examples include the protein-binding problem in computational biology and the Higgs particle-classification problem in high-energy physics. For these problems, quantum-assisted algorithms yield classifiers, trained using a small dataset, with superior accuracies compared to classical algorithms. Quantum-algorithmic performance is deleteriously affected by practical limits,

such as device noise, few qubits and restricted qubit connectivity.

We have proposed a quantum-assisted regression algorithm for the FLD task and tested this algorithm's performance using D-Wave's Hybrid Solver. Our first result is a QUBO formulation for SVR. Specifically, we derive a QUBO form for the constrained optimisation problem involved in training a SVR model. Our second result is a SVR-based FLD algorithm, which solves the multi-output regression task by splitting it into several single-output regression tasks and constructing a SVR model for each such single-output regression problem. Upon implementing this algorithm on D-Wave's Hybrid Solver, we have observed a slight advantage of our hybrid algorithm over classical algorithms in terms of landmark-detection accuracy. Furthermore, we notice that both classical and quantum annealing-based FLD algorithms yield results with lower variances than those obtained using greedy algorithms.

Our work is a proof-of-concept example for applying quantum-assisted SVR to a supervised learning task with a small training dataset. Although we study the vari-

ance of our results to conclude a slight advantage of annealing-based methods over greedy methods, higher-order statistical fluctuations need to be analysed. Some of the possible improvements to the implementations of our FLD algorithm include increasing number of image segments during feature extraction, optimising over annealing hyperparameters and exploring customized workflows for Hybrid Solver. Additionally, future experiments on a larger quantum annealer can utilise quantum annealing exclusively, rather than the quantum-classical hybrid scheme, and yield statistically significant quantum advantages.

ACKNOWLEDGEMENTS

This work is supported by the Major Innovation Fund, Government of Alberta, Canada. We acknowledge the traditional owners of the land on which this work was undertaken at the University of Calgary: the Treaty 7 First Nations.

-
- [1] H. Drucker, C. J. Burges, L. Kaufman, A. J. Smola, and V. Vapnik, Support vector regression machines, in *Advances in neural information processing systems* (MIT Press, 1997) pp. 155–161.
 - [2] A. J. Smola and B. Schölkopf, A tutorial on support vector regression, *Stat. Comput.* **14**, 199 (2004).
 - [3] Y. Radhika and M. Shashi, Atmospheric temperature prediction using support vector machines, *Int. J. Comput. Theory Eng.* **1**, 55 (2009).
 - [4] B. M. Henrique, V. A. Sobreiro, and H. Kimura, Stock price prediction using support vector regression on daily and up to the minute prices, *J. Finance Data Sci.* **4**, 183 (2018).
 - [5] D.-Y. Li, W. Xu, H. Zhao, and R.-Q. Chen, A svr based forecasting approach for real estate price prediction, in *2009 International Conference on Machine Learning and Cybernetics*, Vol. 2 (2009) pp. 970–974.
 - [6] J. Biamonte, P. Wittek, N. Pancotti, P. Rebentrost, N. Wiebe, and S. Lloyd, Quantum machine learning, *Nature* **549**, 195 (2017).
 - [7] V. Dunjko and H. J. Briegel, Machine learning & artificial intelligence in the quantum domain: a review of recent progress, *Rep. Prog. Phys.* **81**, 074001 (2018).
 - [8] T. Kadowaki and H. Nishimori, Quantum annealing in the transverse Ising model, *Phys. Rev. E* **58**, 5355 (1998).
 - [9] A. Mott, J. Job, J.-R. Vlimant, D. Lidar, and M. Spiropulu, Solving a Higgs optimization problem with quantum annealing for machine learning, *Nature* **550**, 375 (2017).
 - [10] R. Y. Li, R. Di Felice, R. Rohs, and D. A. Lidar, Quantum annealing versus classical machine learning applied to a simplified computational biology problem, *npj Quantum Inf* **4**, 14 (2018).
 - [11] D. Willsch, M. Willsch, H. De Raedt, and K. Michielsen, Support vector machines on the D-Wave quantum annealer, *Comput. Phys. Commun.* **248**, 107006 (2020).
 - [12] *D-Wave, Leap's Hybrid Solvers.*
 - [13] N. Wang, X. Gao, D. Tao, H. Yang, and X. Li, Facial feature point detection: A comprehensive survey, *Neurocomputing* **275**, 50 (2018).
 - [14] Y. Wu and Q. Ji, Facial landmark detection: A literature survey, *Int. J. Comput. Vis.* **127**, 115 (2019).
 - [15] I. Masi, F.-J. Chang, J. Choi, S. Harel, J. Kim, K. Kim, J. Leksut, S. Rawls, Y. Wu, T. Hassner, *et al.*, Learning pose-aware models for pose-invariant face recognition in the wild, *IEEE Trans. Pattern Anal. Mach. Intell.* **41**, 379 (2018).
 - [16] X. Zhu, Z. Lei, J. Yan, D. Yi, and S. Z. Li, High-fidelity pose and expression normalization for face recognition in the wild, in *Proceedings of the IEEE conference on computer vision and pattern recognition* (Boston, 2015) pp. 787–796.
 - [17] Y. Taigman, M. Yang, M. A. Ranzato, and L. Wolf, Deepface: Closing the gap to human-level performance in face verification, in *2014 IEEE Conference on Computer Vision and Pattern Recognition* (Columbus, 2014) pp. 1701–1708.
 - [18] J. Choi, G. Medioni, Y. Lin, L. Silva, O. Regina, M. Pamplona, and T. C. Faltemier, 3d face reconstruction using a single or multiple views, in *2010 20th International Conference on Pattern Recognition* (Istanbul, 2010) pp. 3959–3962.
 - [19] B. T. Nguyen, M. H. Trinh, T. V. Phan, and H. D. Nguyen, An efficient real-time emotion detection using camera and facial landmarks, in *2017 Seventh International Conference on Information Science and Technology (ICIST)* (Da Nang, 2017) pp. 251–255.
 - [20] R. Ranjan, V. M. Patel, and R. Chellappa, Hyperface: A deep multi-task learning framework for face detection, landmark localization, pose estimation, and gender recognition, *IEEE Trans. Pattern Anal. Mach. Intell.* **41**,

- 121 (2019).
- [21] Y. Sun, X. Wang, and X. Tang, Deep convolutional network cascade for facial point detection, in *2013 IEEE Conference on Computer Vision and Pattern Recognition* (2013) pp. 3476–3483.
- [22] K. Khabaralakh and L. Koriashkina, Fast facial landmark detection and applications: A survey, [arXiv:2101.10808](https://arxiv.org/abs/2101.10808) (2021).
- [23] B. Scholkopf and A. J. Smola, *Learning with kernels: support vector machines, regularization, optimization, and beyond* (MIT Press, Cambridge, 2018).
- [24] [scikit-learn](https://scikit-learn.org/stable/), [Stochastic Gradient Descent](https://scikit-learn.org/stable/modules/generated/sklearn.linear_model.SGD.html).
- [25] H. Hussain, M. B. Javaid, F. S. Khan, A. Dalal, and A. Khalique, Optimal control of traffic signals using quantum annealing, *Quantum Inf. Process.* **19**, 312 (2020).
- [26] S. Palmer, S. Sahin, R. Hernandez, S. Mugel, and R. Orus, Quantum portfolio optimization with investment bands and target volatility, [arXiv:2106.06735](https://arxiv.org/abs/2106.06735) (2021).
- [27] H. Borchani, G. Varando, C. Bielza, and P. Larrañaga, A survey on multi-output regression, *Wiley Interdiscip. Rev.: Data Min. Knowl. Discov.* **5**, 216 (2015).
- [28] [scikit-learn](https://scikit-learn.org/stable/), [SVR implementation](https://scikit-learn.org/stable/modules/generated/sklearn.svm.SVR.html).
- [29] M. Valstar, B. Martinez, X. Binefa, and M. Pantic, Facial point detection using boosted regression and graph models, in *2010 IEEE Computer Society Conference on Computer Vision and Pattern Recognition* (IEEE, San Francisco, 2010) pp. 2729–2736.
- [30] P. Wittek, *Quantum Machine Learning: What Quantum Computing Means to Data Mining* (Academic Press, Boston, 2014).
- [31] [OpenCV](https://opencv.org/), [Image properties](https://docs.opencv.org/4.x/d4/d13/tutorial_py_image_properties.html).
- [32] P. Viola and M. Jones, Rapid object detection using a boosted cascade of simple features, in *Proceedings of the 2001 IEEE Computer Society Conference on Computer Vision and Pattern Recognition. CVPR 2001*, Vol. 1 (Kauai, 2001) pp. I–I.
- [33] B. Martinez, M. F. Valstar, X. Binefa, and M. Pantic, Local evidence aggregation for regression-based facial point detection, *IEEE Trans. Pattern Anal. Mach. Intell.* **35**, 1149 (2013).
- [34] X. Cao, Y. Wei, F. Wen, and J. Sun, Face alignment by explicit shape regression, *Int. J. Comput. Vis.* **107**, 177 (2014).
- [35] P. Burman, A comparative study of ordinary cross-validation, v-fold cross-validation and the repeated learning-testing methods, *Biometrika* **76**, 503 (1989).
- [36] O. Jesorsky, K. J. Kirchberg, and R. W. Frischholz, Robust face detection using the Hausdorff distance, in *International conference on audio-and video-based biometric person authentication* (Springer, Berlin, 2001) pp. 90–95.
- [37] G. B. Huang, M. Mattar, T. Berg, and E. Learned-Miller, Labeled faces in the wild: A database for studying face recognition in unconstrained environments, in *Workshop on Faces in 'Real-Life' Images: Detection, Alignment, and Recognition* (Marseille, 2008).
- [38] P. N. Belhumeur, D. W. Jacobs, D. J. Kriegman, and N. Kumar, Localizing parts of faces using a consensus of exemplars, *IEEE Trans. Pattern Anal. Mach. Intell.* **35**, 2930 (2013).
- [39] V. Le, J. Brandt, Z. Lin, L. Bourdev, and T. S. Huang, Interactive facial feature localization, in *European conference on computer vision* (Springer, Berlin, 2012) pp. 679–692.
- [40] M. M. Nordström, M. Larsen, J. Sierakowski, and M. B. Stegmann, *The IMM face database-an annotated dataset of 240 face images*, Tech. Rep. (Lyngby, 2004).
- [41] A. Kasinski, A. Florek, and A. Schmidt, The PUT face database, *Image Process. & Commun.* **13**, 59 (2008).
- [42] O. Çeliktutan, S. Ulukaya, and B. Sankur, A comparative study of face landmarking techniques, *EURASIP J. Image Video Process.* **2013**, 1 (2013).
- [43] D. Cristinacce and T. F. Cootes, Feature detection and tracking with constrained local models, in *Proceedings of the British Machine Vision Conference* (BMVA Press, 2006).
- [44] X. Zhu and D. Ramanan, Face detection, pose estimation, and landmark localization in the wild, in *2012 IEEE Conference on Computer Vision and Pattern Recognition* (Providence, 2012) pp. 2879–2886.
- [45] S. Kirkpatrick, C. D. Gelatt, and M. P. Vecchi, Optimization by Simulated Annealing, *Science* **220**, 671 (1983).
- [46] E. Farhi, J. Goldstone, S. Gutmann, and M. Sipser, Quantum computation by adiabatic evolution, [arXiv:quant-ph/0001106](https://arxiv.org/abs/quant-ph/0001106) (2000).
- [47] Z. Bian, F. Chudak, W. G. Macready, and G. Rose, The Ising model: teaching an old problem new tricks, *D-Wave systems* **2** (2010).
- [48] N. Dattani, S. Szalay, and N. Chancellor, Pegasus: The second connectivity graph for large-scale quantum annealing hardware, [arXiv:1901.07636](https://arxiv.org/abs/1901.07636) (2019).
- [49] E. Pelofske, G. Hahn, and H. Djidjev, Solving large minimum vertex cover problems on a quantum annealer, in *Proceedings of the 16th ACM International Conference on Computing Frontiers* (New York, 2019) pp. 76–84.
- [50] J. Cai, W. G. Macready, and A. Roy, A practical heuristic for finding graph minors, [arXiv:1406.2741](https://arxiv.org/abs/1406.2741) (2014).
- [51] [D-Wave](https://docs.dwaveset.com/runtime/tutorial/parameters.html), [Solver parameters: time_limit](https://docs.dwaveset.com/runtime/tutorial/parameters.html).
- [52] N. T. Nguyen, G. T. Kenyon, and B. Yoon, A regression algorithm for accelerated lattice QCD that exploits sparse inference on the D-Wave quantum annealer, *Sci. Rep.* **10**, 10915 (2020).
- [53] T. Potok *et al.*, Adiabatic quantum linear regression, *Sci. Rep.* **11**, 21905 (2021).
- [54] F. Glover, G. Kochenberger, and Y. Du, A tutorial on formulating and using QUBO models, [arXiv:1811.11538](https://arxiv.org/abs/1811.11538) (2019).
- [55] [D-Wave](https://docs.dwaveset.com/runtime/tutorial/dwave_neal.html), [dwave-neal](https://docs.dwaveset.com/runtime/tutorial/dwave_neal.html).
- [56] http://mmlab.ie.cuhk.edu.hk/archive/CNN_FacePoint.htm#ref (2013).
- [57] [OpenCV](https://docs.opencv.org/4.x/d4/d13/tutorial_py_image_properties.html), [Colour conversion](https://docs.opencv.org/4.x/d4/d13/tutorial_py_image_properties.html).
- [58] [OpenCV](https://docs.opencv.org/4.x/d4/d13/tutorial_py_image_properties.html), [Resize image](https://docs.opencv.org/4.x/d4/d13/tutorial_py_image_properties.html).
- [59] T. Ahonen, A. Hadid, and M. Pietikainen, Face description with local binary patterns: Application to face recognition, *IEEE Trans. Pattern Anal. Mach. Intell.* **28**, 2037 (2006).
- [60] [scikit-image](https://scikit-image.org/), [local binary patterns](https://scikit-image.org/docs/0.16.x/api/skimage.filters.local_binary_patterns.html).
- [61] R. Parekh, *Fundamentals of Image, Audio, and Video Processing Using MATLAB: With Applications to Pattern Recognition* (CRC Press, Boca Raton, 2021).
- [62] [scipy](https://docs.scipy.org/doc/scipy/), [Pearson correlation coefficient](https://docs.scipy.org/doc/scipy/reference/generated/scipy.stats.pearsonr.html).
- [63] C.-C. Chang and C.-J. Lin, LIBSVM: A library for support vector machines, *ACM Trans. Intell. Syst. Technol.* **2** (2011).
- [64] [D-Wave](https://docs.dwaveset.com/runtime/tutorial/parameters.html), [Solver properties: minimum_time_limit](https://docs.dwaveset.com/runtime/tutorial/parameters.html).

Appendix A: Computing the offset in prediction function

In this appendix, we provide a comprehensive overview of the methods used in the LIBSVM library [63, p. 10] for computing the offset b in the prediction function (17). In this method, the Karush-Kuhn-Tucker (KKT) conditions are employed to derive bounds for b and estimate its value. We begin by discussing the KKT conditions and their implications for a linear prediction function (10). These conditions yield general bounds for b . Finally, we provide two methods used for estimating b in practice.

The KKT conditions are constraints required to obtain optimal solutions. These conditions govern the relations between the dual variables (α^+ , α^-) and the constraints in the primal formulation (6). Given a data point (\mathbf{x}_i, y_i) and a particular solution $f_{\text{linear}}(\mathbf{x}_i) = \mathbf{w} \cdot \mathbf{x}_i + b$, the KKT conditions are [2, Eqs. (12,13)]

$$\alpha_i^+ (\varepsilon + \xi_i^+ - y_i + \mathbf{w} \cdot \mathbf{x}_i + b) = 0, \quad (\text{A1})$$

$$\alpha_i^- (\varepsilon + \xi_i^- + y_i - \mathbf{w} \cdot \mathbf{x}_i - b) = 0, \quad (\text{A2})$$

$$\xi_i^+ (\gamma - \alpha_i^+) = 0, \quad (\text{A3})$$

$$\xi_i^- (\gamma - \alpha_i^-) = 0. \quad (\text{A4})$$

By Fig. 1, we construct mathematical conditions for the data point to be inside or outside the ε -insensitive tube. Inside the tube, the data point can be either above or below the line representing the prediction function, as expressed by the relations

$$y_i - f_{\text{linear}}(x_i) \leq \varepsilon, \quad \xi_i^+ = 0, \quad (\text{A5})$$

and

$$-\varepsilon \leq y_i - f_{\text{linear}}(x_i), \quad \xi_i^- = 0, \quad (\text{A6})$$

respectively. If the point resides outside the tube, it can either be above the upper margin, with

$$y_i - f_{\text{linear}}(x_i) - \varepsilon \geq 0, \quad (\text{A7})$$

or below it, for

$$y_i - f_{\text{linear}}(x_i) + \varepsilon \leq 0. \quad (\text{A8})$$

Using the set of KKT conditions, one can derive the upper and lower bounds for b . For $\alpha_i^+ < \gamma$, $\xi_i^+ = 0$ by Eq. (A3), and the corresponding datapoint is inside the tube (A5). Additionally, $\alpha_i^+ > 0$ implies that the expression inside parenthesis in Eq. (A1) needs to be zero and, consequently, the point is outside the tube (A7). Similarly for $\alpha_i^- < \gamma$, we can infer that $\xi_i^- = 0$ (A4) and the point is inside the tube (A6). For the case when $\alpha_i^- > 0$, Eq. (A2) suggests that the point is outside the tube and below the lower margin (A8). Based on these observations, we can concisely state the bounds for b as [63]

$$\begin{aligned} \max\{b_i^- \mid \alpha_i^+ < \gamma \text{ or } b_i^+ \mid \alpha_i^- > 0\} \leq b \leq \\ \min\{b_i^- \mid \alpha_i^+ > 0 \text{ or } b_i^+ \mid \alpha_i^- < \gamma\} \quad \forall i \in [M], \end{aligned} \quad (\text{A9})$$

with

$$b_i^\pm := \pm \varepsilon + y_i - \sum_{j=0}^{M-1} (\alpha_j^+ - \alpha_j^-) \mathbf{x}_j \cdot \mathbf{x}_i. \quad (\text{A10})$$

We now describe the methods used in the LIBSVM library [63, p. 10] for computing b . If there exists at least one α_i^+ or α_i^- that lies in the interval $(0, \gamma)$, the inequalities in Eq. (A9) become equalities, and b is estimated as the average

$$b = \frac{\sum_{i:\alpha_i^+ \in (0,\gamma)} b_i^- + \sum_{i:\alpha_i^- \in (0,\gamma)} b_i^+}{|\{i \mid \alpha_i^+ \text{ or } \alpha_i^- \in (0, \gamma)\}|}. \quad (\text{A11})$$

For the case where no α_i^+ or α_i^- is in the interval $(0, \gamma)$, the bounds in Eq. (A9) simplifies to

$$\begin{aligned} \max\{b_i^- \mid \alpha_i^+ = 0 \text{ or } b_i^+ \mid \alpha_i^- = \gamma\} \leq b \leq \\ \min\{b_i^- \mid \alpha_i^+ = \gamma \text{ or } b_i^+ \mid \alpha_i^- = 0\}, \end{aligned} \quad (\text{A12})$$

and b is estimated to be the midpoint of this range. In the non-linear prediction function (17), we use $K(\mathbf{x}_j, \mathbf{x}_i)$ instead of $\mathbf{x}_j \cdot \mathbf{x}_i$ in the calculations of b_i^+ and b_i^- .

Appendix B: QUBO formulation for SVR

In this appendix, we establish an expression for elements of the QUBO matrix \tilde{Q} (40) in QUBO formulation of a SVR. To make the established expression symmetric, we treat the squared-penalty term in the objective function in Eq. (56) as a product of two similar terms. Expanding the objective function $\mathcal{L}(\alpha)$ yields

$$\begin{aligned} \mathcal{L}(\alpha) = & \frac{1}{2} \sum_{n,m=0}^{2M-1} \alpha_n Q_{nm} \alpha_m + \sum_{m=0}^{2M-1} \alpha_m c_m \\ & + \lambda \left(\sum_{m=0}^{M-1} \alpha_m \right)^2 + \lambda \left(\sum_{m=M}^{2M-1} \alpha_m \right)^2 \\ & - \lambda \sum_{m=0}^{M-1} \sum_{n=M}^{2M-1} \alpha_m \alpha_n - \lambda \sum_{m=M}^{2M-1} \sum_{n=0}^{M-1} \alpha_m \alpha_n. \end{aligned} \quad (\text{B1})$$

To obtain a binary form, we substitute the real-to-binary encoding in Eq. (41) into this objective function, and

expand the quadratic terms. We then obtain

$$\begin{aligned}
\mathcal{L}(\mathbf{a}) = & \frac{1}{2^{2B_f+1}} \sum_{n,m=0}^{2M-1} \sum_{i,j=0}^{B-1} 2^{i+j} a_{Bn+i} Q_{nm} a_{Bm+j} \\
& + \frac{1}{2^{B_f}} \sum_{n=0}^{2M-1} \sum_{i=0}^{B-1} 2^i c_n a_{Bn+i} \\
& + \frac{\lambda}{2^{2B_f}} \sum_{n,m=0}^{M-1} \sum_{i,j=0}^{B-1} 2^{i+j} a_{Bn+i} a_{Bm+j} \\
& + \frac{\lambda}{2^{2B_f}} \sum_{n,m=M}^{2M-1} \sum_{i,j=0}^{B-1} 2^{i+j} a_{Bn+i} a_{Bm+j} \\
& - \frac{\lambda}{2^{2B_f}} \sum_{m=0}^{M-1} \sum_{n=M}^{2M-1} \sum_{i,j=0}^{B-1} 2^{i+j} a_{Bn+i} a_{Bm+j} \\
& - \frac{\lambda}{2^{2B_f}} \sum_{m=M}^{2M-1} \sum_{n=0}^{M-1} \sum_{i,j=0}^{B-1} 2^{i+j} a_{Bn+i} a_{Bm+j}. \quad (\text{B2})
\end{aligned}$$

To fit the QUBO form, we express this equation as

$$\mathcal{L}(\mathbf{a}) = \mathbf{a}^\top \tilde{\mathbf{Q}} \mathbf{a} = \sum_{n,m=0}^{2M-1} \sum_{i,j=0}^{B-1} a_{Bn+i} \tilde{Q}_{Bn+i, Bm+j} a_{Bm+j}, \quad (\text{B3})$$

where $\tilde{\mathbf{Q}}$ is the QUBO matrix with size $2MB \times 2MB$.

Then by Eqs. (B2), (58) and (59), we have

$$\begin{aligned}
\tilde{Q}_{Bn+i, Bm+j} = & \frac{1}{2} \frac{2^{i+j}}{2^{2B_f}} Q_{nm} + \frac{2^i}{2^{B_f}} \delta_{nm} \delta_{ij} c_n \\
& + \lambda \frac{2^{i+j}}{2^{2B_f}} (\bar{\Theta}(n-M) \bar{\Theta}(m-M)) \\
& + \lambda \frac{2^{i+j}}{2^{2B_f}} (\Theta(n-M) \Theta(m-M)) \\
& - \lambda \frac{2^{i+j}}{2^{2B_f}} \bar{\Theta}(m-M) \Theta(n-M) \\
& - \lambda \frac{2^{i+j}}{2^{2B_f}} \bar{\Theta}(n-M) \Theta(m-M). \quad (\text{B4})
\end{aligned}$$

The combination of this equation and the identity

$$\bar{\Theta}(i) \bar{\Theta}(j) + \Theta(i) \Theta(j) = 1 - \bar{\Theta}(i) \Theta(j) - \bar{\Theta}(j) \Theta(i), \quad (\text{B5})$$

for any $i, j \in \mathbb{Z}$, yields the expression

$$\begin{aligned}
\tilde{Q}_{Bn+i, Bm+j} = & \frac{1}{2} \frac{2^{i+j}}{2^{2B_f}} Q_{nm} + \frac{2^i}{2^{B_f}} \delta_{nm} \delta_{ij} c_n + \lambda \frac{2^{i+j}}{2^{2B_f}} \\
& - 2\lambda \frac{2^{i+j}}{2^{2B_f}} \bar{\Theta}(m-M) \Theta(n-M) \\
& - 2\lambda \frac{2^{i+j}}{2^{2B_f}} \bar{\Theta}(n-M) \Theta(m-M), \quad (\text{B6})
\end{aligned}$$

for elements of the QUBO matrix.

Appendix C: Detailed results

Here we present detailed numerical results of our experiments. We state the optimal hyperparameter tuples in Eqs. (52) and (53) for the three ε -SVR models, namely SKL-landmark, SA-landmark and QA-landmark. Additionally, we provide the exact numerical values used to make the plots in Fig. 5 and Fig. 6 for performance comparison.

LFW	SKL			SA			QA		
	Landmark #	(γ, η)	MNDE	FR	(K, η, ξ)	MNDE	FR	(K, η, ξ)	MNDE
1	(31,16)	4.19 (0.27)	0	(5,16,1)	4.02 (0.25)	4	(4,16,1)	3.88 (0.25)	0
	(15,16)			(6,4,10)			(4,16,10)		
2	(63,4)	4.14 (0.28)	4	(6,4,5)	4.14 (0.28)	4	(5,16,10)	4.18 (0.28)	4
	(31,64)			(4,64,10)			(5,16,10)		
3	(63,16)	6.03 (0.33)	16	(6,64,10)	6.07 (0.33)	16	(4,64,5)	5.95 (0.31)	8
	(15,64)			(5,16,1)			(4,64,5)		
4	(63,64)	5.42 (0.39)	12	(5,256,10)	5.22 (0.38)	12	(4,256,5)	5.21 (0.38)	12
	(63,4)			(4,16,5)			(4,4,1)		
5	(15,64)	6.28 (0.33)	12	(5,64,5)	6.24 (0.31)	12	(5,16,10)	6.29 (0.31)	16
	(63,4)			(5,16,5)			(4,64,10)		
1-5	-	5.21 (0.33)	8.8	-	5.14 (0.33)	9.6	-	5.1 (0.32)	8

TABLE I. Optimal hyperparameter tuples (with $\varepsilon = 0.1$ and $B_f = 0$) and performance estimations for three ε -SVR models. For each model, we state MNDE in % and FR in %, calculated for the LFW test dataset. The standard deviation of normalised detection errors is shown in parentheses beside each MNDE value. These values are used in Fig. 5.

LFPW	SKL		SA		QA		BoRMaN	
Landmark #	MNDE	FR	MNDE	FR	MNDE	FR	MNDE	FR
1	5.10 (0.28)	4.27	5.14 (0.28)	3.66	5.23 (0.28)	4.27	3.63 (0.38)	5.49
2	4.53 (0.32)	7.92	4.67 (0.31)	7.32	4.77 (0.32)	7.93	3.82 (0.38)	6.1
3	7.21 (0.54)	23.17	6.92 (0.44)	22.56	6.81 (0.45)	21.95	6.66 (0.57)	22.56
4	6.78 (0.34)	18.9	6.85 (0.35)	20.12	6.73 (0.34)	17.68	5.94 (0.48)	15.24
5	7 (0.34)	18.29	7.11 (0.33)	16.46	7.3 (0.34)	17.07	6.17 (0.46)	15.85
1-5	6.12 (0.37)	14.51	6.14 (0.36)	14.02	6.17 (0.36)	13.78	5.24 (0.48)	13.05

BioID	SKL		SA		QA		BoRMaN	
Landmark #	MNDE	FR	MNDE	FR	MNDE	FR	MNDE	FR
1	4.25 (0.26)	2.68	4.33 (0.26)	2.61	4.42 (0.26)	2.83	3.56 (0.39)	5.59
2	3.61 (0.22)	1.19	3.82 (0.23)	1.71	3.84 (0.23)	1.49	3.89 (0.38)	5.89
3	6.57 (0.34)	14.47	6.22 (0.35)	12.82	5.94 (0.33)	10.51	5.56 (0.49)	13.79
4	5.79 (0.33)	11.56	5.64 (0.33)	10.66	5.51 (0.33)	10.44	4.72 (0.44)	9.99
5	4.89 (0.33)	7.68	4.83 (0.32)	7.23	4.9 (0.32)	6.93	5.36 (0.49)	13.94
1-5	5.02 (0.32)	7.52	4.97 (0.31)	7	4.92 (0.30)	6.44	4.62 (0.45)	9.84

TABLE II. Summary of performance estimations for our three ε -SVR models and the model constructed using BoRMaN algorithm. These values are used for plotting Fig. 6.